

# **CHARGE COLLECTION MECHANISMS IN A SUB-MICRON GRATED MSM PHOTODETECTOR: FIELD ANALYSIS**

---

A Thesis presented to the faculty of the Graduate School  
University of Missouri-Columbia

---

In Partial Fulfillment  
Of the Requirements for the Degree  
Master of Science

---

by  
SURESH KRANTHI NAKKA

Dr. Naz E. Islam, Thesis Supervisor

JULY 2005

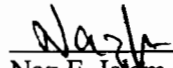
The undersigned, appointed by the Dean of the Graduate School,  
have examined the thesis entitled.

**CHARGE COLLECTION MECHANISMS IN A SUB-MICRON  
GRADED MSM PHOTODETECTOR: FIELD ANALYSIS**

Presented by Suresh Kranthi Nakka

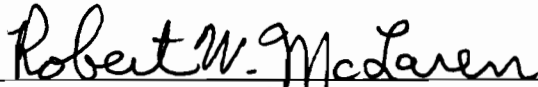
A candidate for the degree of Master of Science

And hereby certify that in their opinion it is worthy of acceptance.



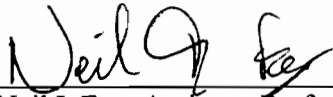
---

Naz E. Islam, Associate Professor, Dept. of Electrical and Computer Engineering



---

Robert W. McLaren, Professor Emeritus, Dept. of Electrical and Computer Engineering



---

Neil I. Fox, Assistant Professor, Dept. of Soil, Environmental and Atmospheric Sciences

## **ACKNOWLEDGEMENTS**

I would like to acknowledge the help of many people during my course of study. Firstly, I would like to thank my advisor Dr. Naz E. Islam for providing invaluable insights, timely encouragement as well as guidance, balanced by the freedom to express myself throughout this research work. I am thankful to Dr. Robert McLaren and Dr. Neil Fox who readily agreed to be members of my thesis examining committee. I would like to extend my sincere thanks to Dr. Phumin Kirawanich for many insightful conversations and helpful comments which made this thesis possible.

In the race against the clock in which one almost inevitably becomes enmeshed when preparing a thesis, it is a true relief to be surrounded by people who show sympathy and who continue to believe in what you are doing. The credit for such support goes to my friends and colleagues, whose inspiring interest and ceaseless enthusiasm for the topic explored in this thesis has meant a great deal to me. Finally, I dedicate this work to my parents and sisters. Without their love, understanding, endless patience, support and encouragement this work could not have been accomplished.

## TABLE OF CONTENTS

ACKNOWLEDGEMENTS.....	ii
LIST OF ILLUSTRATIONS.....	v
LIST OF SYMBOLS.....	vii
CHAPTER	
1. INTRODUCTION.....	1
2. BACKGROUND.....	5
2.1 Photodetector.....	5
2.1.1 Performance Criterion for a Good Photodetector.....	6
2.2 Metal Semiconductor Metal (MSM) Photodetector.....	6
2.3 Electromagnetic Wave Fundamentals.....	11
2.3.1 Electromagnetic Waves.....	11
2.3.2 Wave Equation.....	12
2.3.3 Propagation of Electromagnetic Waves.....	15
2.4 Reflection and Transmission of an Electromagnetic Wave.....	17
2.4.1 Normal Incidence on a Lossless Dielectric.....	17
2.4.2 Oblique Incidence at a Dielectric Boundary.....	21
2.4.2.1 Perpendicular Polarization.....	22

2.4.2.2 Parallel Polarization.....	25
2.5 Energy Transported by the EM Waves.....	28
3. LITERATURE REVIEW.....	30
4. THE SIMULATION METHOD.....	37
4.1 Introduction.....	37
4.2 The Finite Integration Technique (FIT).....	39
4.3 Implementation of FIT Equations into Simulation Software.....	43
4.3.1 Transient Solver.....	44
4.3.2 Eigenmode Solver.....	45
4.3.3 Modal Analysis Solver.....	46
4.3.4 Frequency Domain Solver.....	47
5. RESEARCH APPROACH.....	49
5.1 Introduction.....	49
5.2 Analysis of Square and Wall like Grating Structures.....	50
5.3 Analysis of Square Gratings with Change in Area.....	57
5.4 Analysis of Cone like Grating Structures.....	60
5.5 Analysis of Square Gratings with Cladding.....	64
6. CONCLUSIONS.....	69
7. REFERENCES.....	71

## LIST OF ILLUSTRATIONS

Figure	Page
2.1 General Structure of a MSM Photodetector .....	7
2.2 Basic Schematic of an Interdigitated MSM Photodetector.....	8
2.3 Topology of the Electromagnetic Waves.....	11
2.4 Spatial Variations of E and H Fields for an EM Wave traveling in z- direction.....	14
2.5 Uniform plane wave normally incident on a lossless dielectric boundary.....	17
2.6 A perpendicularly polarized wave incident on a dielectric boundary.....	23
2.7 A parallel polarized wave at a dielectric boundary.....	26
4.1 Allocation of the grid voltages and facet fluxes on the primary and dual grids.....	40
4.2 Time derivative of the magnetic flux defined on the enclosed primary cell facet.....	41
5.1 Simulated structure without any gratings.....	50
5.2 Input excitation signal (continuous sine wave).....	51
5.3 Incident wave amplitude changes as it travels through the surface of the detector without any gratings.....	51
5.4 Simulated Structure for (a) walls and, (b) square Gratings.....	52
5.5 Incident wave amplitude changes as it travels from the wall-like grating to the substrate regions.....	53
5.6 Incident wave amplitude changes as it travels from the square grating to the substrate regions.....	54

5.7	Single wall grating on the active region used for analysis.....	55
5.8	Front View of the Simulated Structure with different Si extension areas.....	57
5.9	Incident wave amplitude changes for a wave traveling through different Si extension areas.....	58
5.10	Plot of the E-field vs number of spikes.....	59
5.11	Simulated structure with cone gratings.....	60
5.12	Incident wave amplitude changes as it travels through cone and square gratings.....	61
5.13	Analysis of (a) cone and, (b) square grating structures.....	62
5.14	Simulated Structure with doping around the square gratings.....	64
5.15	Incident wave amplitude changes as it travels through square gratings with and without doping (coating).....	65
5.16	Guiding of waves in a square grating.....	66

## LIST OF SYMBOLS

Symbol	Physical Quantity	Unit
$\psi$	Electrostatic Potential	Volt, V
$q$	Electron charge	Coulomb, C
$c$	Speed of light	Meters per sec, m/s
$k$	Propagation constant/wave number	Radians per meter, rad/m
$\lambda$	Wavelength	Meter, m
$f$	Frequency	Hertz, Hz
$E$	Electric field Intensity	Volts per meter, V/m
$H$	Magnetic Field Intensity	Ampere per meter, A/m
$D$	Electric Flux Density	Coulomb per square meter, C/m <sup>2</sup>
$B$	Magnetic Flux Density	Tesla, T
$\mu$	Permeability	Henry per meter, H/m
$\varepsilon$	Permittivity	Farad per meter, F/m
$J_c$	Current Density	Ampere per square meter, A/m <sup>2</sup>
$\rho_v$	Volume charge density	Coulomb per cubic meter, C/m <sup>3</sup>
$S$	Poynting Vector	Watts per square meter, W/m <sup>2</sup>
$S_{av}$	Power Density	Watts per square meter, W/m <sup>2</sup>
$\sigma$	Conductivity	Siemens per meter, S/m



$\eta$	Intrinsic Impedance	Ohm, $\Omega$
$\omega$	Angular Frequency	Radians per second, rad/s
$n$	Refractive Index	-----
$\Gamma$	Reflection Coefficient	-----
$\tau$	Transmission Coefficient	-----
$Z$	Characteristic Impedance	Ohm, $\Omega$
$\theta_i$	Angle of Incidence	Electrical Degrees, $^\circ$
$\theta_r$	Angle of Reflection	Electrical Degrees, $^\circ$
$\theta_t$	Angle of Transmission	Electrical Degrees, $^\circ$

# **CHAPTER 1**

## **INTRODUCTION**

A Photodetector is a semiconductor device that absorbs optical energy and converts it to electrical energy, which usually manifests as a photocurrent. It is a key component in optical transmission and measurement systems. Photodetectors are important in optical-fiber communication systems in the near-infrared region. They demodulate optical signals, that is, convert the optical variations into electrical variations, which are subsequently amplified and further processed. For such applications, photodetectors must satisfy stringent requirements such as high sensitivity at operating wavelengths, high response speed, and maximum efficiency.

High efficiency and low-power photodetectors (PD's) are always sought after in both long-haul and local area communication systems. High speed PD's are used in a wide range of microwave photonics applications from fiber optic communication lines and optical wireless systems to photonic measurement systems for detection and conversion of optical signals, and for microwave generation, as well as for optical control of microwave circuits and devices.

Photodetectors are a critical component in light wave systems. As data rates increase, implementing high-quantum efficient, short response time, low capacitance (for input to receivers), and large-area (for sensitivity and alignment tolerance) photodetectors

becomes a critical issue. However, high efficiency, short response time, and a large detection area involve tradeoffs that must be intelligently optimized.

A special kind of photodetector called the Metal Semiconductor Metal (MSM) photodetector is attractive for many optoelectronic applications, such as optical communications, future high-speed chip-to-chip connection, and high-speed sampling, because of their high sensitivity-bandwidth product and their compatibility with large-scale planar integrated circuit (IC) technology.

The electrodes of the MSM photodetector are often interdigitated to increase the active region area, while optimizing the electric fields in the carrier collection region. An increase in the collection efficiency of Si MSM photodetectors therefore would make these devices more attractive for a wide variety of applications. One process to increase the collection efficiency of the MSM photodetectors is to use wall-like grated structures of submicron dimensions on the photodetector. This concept is used as a benchmark for this project.

An increase in charge collection efficiency of a MSM Photodetector can be analyzed through two different methods: one is the semiconductor approach and other is the electromagnetic approach. In this project, the electromagnetic approach was chosen as the simulation tool.

The main objective of this project is to perform electromagnetic field analysis to explain the improved collection efficiency of grating photodetectors. This analysis of a Si MSM photodetector is performed by looking into the transmission of electromagnetic wave field components as they travel through the grating structures on the detector into the device's active region. Here, it is shown that there is an increase in the collection efficiency for one given wavelength of the incident electromagnetic signal when the wall-like grating structures on the detector are changed to a square lattice.

The variations in the amplitude of the electric field intensity of the photodetector were determined by changing the area covered by the Si gratings on the detector. All the simulations were done using the CST Microwave Studio software which is based on the Finite Integration Technique.

This thesis is comprised of six chapters which are organized as follows. Chapter 2 provides the background of a photodetector and its basics. It explains the performance criteria of a good photodetector. This is followed by a discussion of a special kind of detector called an MSM Photodetector and its functioning. The fundamentals of electromagnetic waves and the energy transported by these waves are also presented. Finally, the reflection and transmission of the EM waves between two media together with equations related to the efficiency of the EM waves for the case of normal and oblique incidence are presented in detail.

Chapter 3 summarizes previous research work done on the MSM photodetectors. It talks about the various attempts involved to increase the efficiency of an MSM photodetector.

Chapter 4 starts with the introduction of different numerical techniques used to solve the complicated electromagnetic problems, followed by a brief introduction of the Finite Integration Technique (FIT). This chapter ends with the incorporation of the appropriate equations into the software used for the analysis.

Chapter 5 deals with the simulation setup and the results obtained. The research work done to increase the charge collection efficiency of the MSM photodetector is also discussed. It is shown that the square-like gratings improve the efficiency of the photodetector, as compared to a wall-like structure in the active region. Simulation results along with explanations for the case of variations in the number of Si gratings and variations in its dimensions are also presented.

Finally, in Chapter 6, conclusions are drawn and some ideas for further study are discussed.

## **CHAPTER 2**

### **BACKGROUND**

#### **2.1 Photodetector**

Photodetectors are used in many applications of everyday life, from the bar code scanner at the grocery store to the receiver for a remote control on a VCR, as well as the photoreceiver at the end of a fiber optic cable in an optical communication system. A photodetector is an optoelectronic device that absorbs optical energy and converts it to electrical energy, which usually manifests as a photocurrent. There are generally three steps involved in the photodetection process:

- 1) Absorption of optical energy and generation of carriers
- 2) Transportation of photogenerated carriers across the absorption and/or transit region
- 3) Carrier collection and generation of a photocurrent, which flows through external circuitry

The process of photodetection is sometimes associated with demodulation, when a high-frequency optical signal is converted into a time-varying electrical signal and further processed and rectified. Photodetectors are used to detect optical signals ranging over a very wide range of the optical spectrum. The high data rate of the present day optical fiber transmission systems imposes severe demands on the response speed of the photodetector. In this application, detectors should receive the transmitted optical pulses

and convert them, with as little loss as possible, into electronic pulses that can be used by a telephone, a computer, or other terminal at the receiving end.

### **2.1.1 Performance Criterion for a Good Photodetector**

A photodetector must satisfy very stringent requirements for effective performance and compatibility. The main performance criteria for good photodetectors are:

1. High sensitivity at the operating wavelengths
2. High fidelity
3. Large optical to electrical conversion efficiency
4. High response speed
5. Large SNR at the output
6. High reliability
7. Low sensitivity of performance to ambient conditions

Because the photodetector is only a part of the whole optoelectronic receiver system, most of which is electronic in nature, the design of the detector should be compatible with the design and architecture of the rest of the system. This compatibility requires that the detector should have a small-size, a low-bias voltage, and can be easily integrated into the receiver system.

## **2.2 Metal Semiconductor Metal (MSM) Photodetector**

Metal-Semiconductor-Metal (MSM) photodetectors are a special kind of photodetectors which are attractive for many optoelectronic applications including the next generation of

high performance optical communication interconnects. MSM's are simple to fabricate and are compatible with VLSI technology. MSM PD's have simple device technology, fast response, small capacitance and a large active area. Metal Semiconductor Metal (MSM) photodetector basically consists of two Schottky barriers connected back to back as shown in Fig. 2.1. Light is received at the gap between the metal contacts, and the MSM photodetector avoids absorption of light by the metal layer as in a conventional Schottky photodiode. For compound semiconductors, the light absorption layer is usually deposited on a semi-insulating substrate.

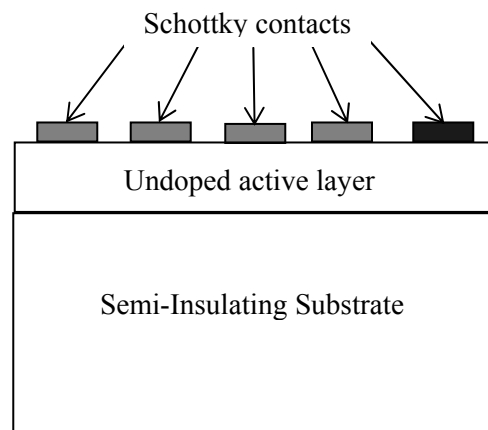


**Fig. 2.1 General Structure of a MSM Photodetector**

Metal-semiconductor-metal (MSM) photodetectors offer an attractive benefit over alternative photodetectors, such as conventional p-i-n photodiodes. An MSM photodetector is inherently planar and requires only a single photolithography step, which is compatible with existing field effect transistor (FET) technology. MSM photodetectors are very high speed devices due to their low capacitance, and they typically have very low dark currents (current produced without incident light). However, the responsivity



(total signal produced from a given optical input) is quite low compared to p-i-n photodiodes. The main causes for the low responsivity is the reflection from the metal surface and semiconductor surface, the finite carrier lifetime as the carriers traverse the gap between the electrodes before being collected, absorption of incident light outside the region in which photogenerated carriers can be collected by the electrodes, and surface recombination currents and deep traps within the semiconductor material, which may lower the detected optical signal.

MSM photodiodes have a much lower capacitance per unit area than p-i-n photodiodes and thus are often transit-time limited. The transit time is related to the spacing between interdigitated electrodes. A MSM photodiode can be used to improve the feasibility of fabricating optoelectronic integrated circuits (OEIC's) for a fiber optic communication system because of its simple and compatible fabrication process. The basic structure of an interdigitated MSM photodetector is shown in Figure 2.2.

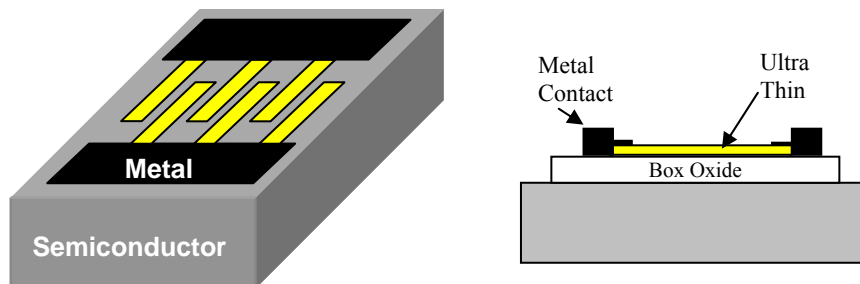


**Fig 2.2 Basic Schematic of an Interdigitated MSM Photodetector**

The integrability of MSM photodiodes with pre-amplifier circuitry comes from the fact that

1. MSM photodiodes do not require doping, which eliminates any parasitic capacitive coupling between the photodiode and the doped regions within the active transistors; and
2. The Schottky electrodes of the MSM photodiodes are essentially identical to gate metallization of field effect transistors (FET's).

MSM photodetectors suffer from very low quantum efficiencies also because the metallization for the electrodes shadows the active light collecting region. Shadowing can limit the incident light from reaching the active region of the MSM detector and prevents the quantum efficiency from being more than 50% for equal electrode widths and spacing. There are design trade-offs in MSM photodiodes for optimizing the speed and quantum efficiency. The average carrier transit time in an MSM photodiode can be decreased by reducing the absorption layer thickness, increasing the applied bias, or reducing the interdigitated electrode spacings.

However, a decrease in the absorption layer thickness results in the degradation of responsivity; a decrease in the electrode spacing leads to a degradation of the dark current and the breakdown voltage and the requirement for complex lithography. An analysis of the energy transported in a MSM Photodetector is possible through two different methods. One is the semiconductor approach and other is the electromagnetic approach.

In the semiconductor approach the three basic equations that provide the general framework for the charge transport are

**Poisson's Equation:**

$$\text{div}(\varepsilon \nabla \psi) = -\rho \quad (2.1)$$

**Carrier Continuity Equations**

$$\frac{\partial n}{\partial t} = \frac{1}{q} \text{div} J_n + G_n - R_n \quad (2.2)$$

$$\frac{\partial p}{\partial t} = \frac{1}{q} \text{div} J_p + G_p - R_p \quad (2.3)$$

Where,

$\psi$  = Electrostatic potential,

$\rho$  = Space charge density,

$q$  = Magnitude of the charge on an electron,

$n$  and  $p$  = electron and hole concentrations respectively,

$J_n$  and  $J_p$  = electron and hole current densities,

$G_n$  and  $G_p$  = Generation rate of electron and holes,

$R_n$  and  $R_p$  = Recombination rates for electrons and holes,

In addition, secondary equations are used to specify particular physical models for electron and hole generation, recombination rates and current densities. The analysis of the energy transported in a MSM photodetector can also be done using electromagnetic approach. In this project, the electromagnetic approach is chosen as the simulation tool.

## 2.3 Electromagnetic Wave Fundamentals

### 2.3.1 Electromagnetic Waves

James C. Maxwell (1831-1879) published his Electromagnetic Field Equations in 1864. He brought together previous experimental work and concepts of Gauss, Ampere and Faraday, as well as his own knowledge of mathematics to present this analysis of electromagnetic fields. With his field equations, Maxwell calculated the speed of electromagnetic propagation to be the same as the speed of light, which indicated that light is also an electromagnetic field. Fig. 2.3 shows the basic topology of Electromagnetic waves. Maxwell's equations are the basis for the theory of electromagnetic fields and waves. They are used in the design of antennas, transmission lines, cavity resonators, fiber optics and solving radiation problems.

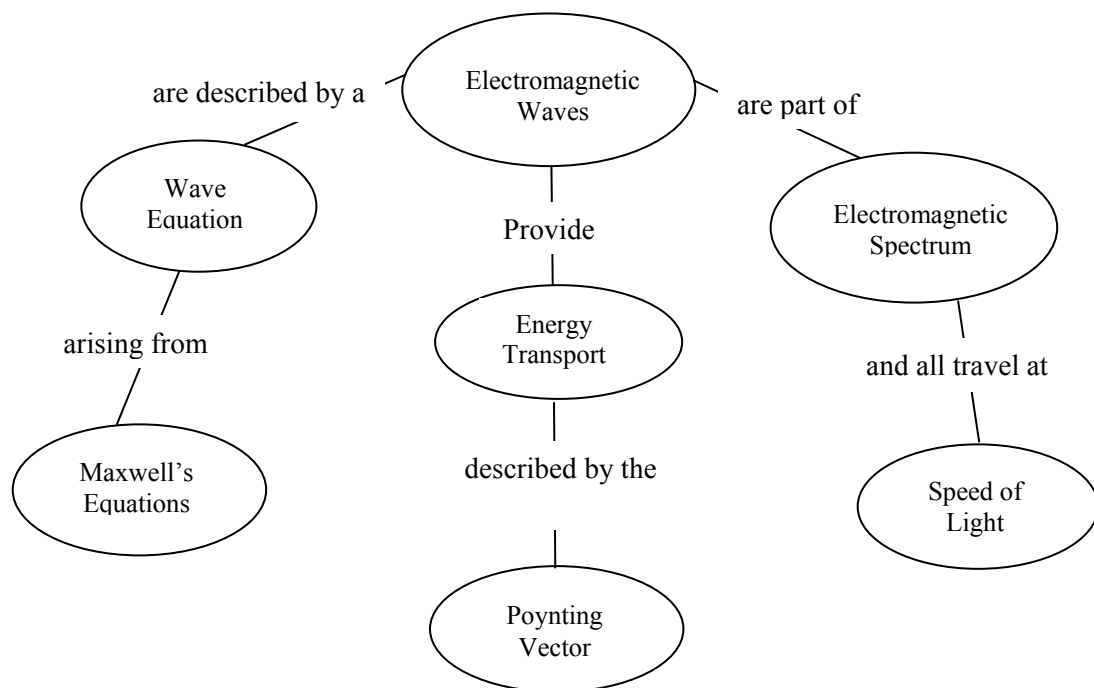


**Fig 2.3 Topology of the Electromagnetic Waves**

### 2.3.2 Wave Equation

The Maxwell's equations in differential form are given below

$$\nabla \times E = -\mu \frac{\partial H}{\partial t} \quad (2.4)$$

$$\nabla \times H = J_c + \varepsilon \frac{\partial E}{\partial t} \quad (2.5)$$

$$\nabla \cdot D = \rho_v \quad (2.6)$$

$$\nabla \cdot B = 0 \quad (2.7)$$

Where, E is Electric Field intensity (V/m), H is the magnetic field intensity (A/m), D is the Electric Flux Density (C/m<sup>2</sup>), B is the Magnetic Flux Density (T),  $\mu$  is the permeability (H/m),  $\varepsilon$  is the permittivity (F/m),  $J_c$  is the current density (A/m<sup>2</sup>), and  $\rho_v$  is the Volume charge density (C/m<sup>3</sup>).

In free space or a lossless dielectric, Eqs. 2.5 and 2.6 become

$$\nabla \times H = \varepsilon \frac{\partial E}{\partial t} \quad (2.8)$$

$$\nabla \cdot D = \nabla \cdot E = 0 \quad (2.9)$$

Then, by taking the curl of Equation 2.4 and substituting into Eq. 2.8,

$$\nabla \times (\nabla \times E) = -\mu \left( \nabla \times \frac{\partial H}{\partial t} \right) = -\mu \varepsilon \frac{\partial^2 E}{\partial t^2} \quad (2.10)$$

But, 
$$\nabla \times (\nabla \times E) = \nabla(\nabla \cdot E) - \nabla^2 E \quad (2.11)$$

$$\nabla \times (\nabla \times E) = \nabla(\nabla \cdot E) - \nabla^2 E = -\mu \varepsilon \frac{\partial^2 E}{\partial t^2} \quad (2.12)$$

Hence,

$$\nabla^2 E = \mu\epsilon \frac{\partial^2 E}{\partial t^2} \quad \text{V/m}^3 \quad (2.13)$$

When expanded in Cartesian coordinates, Eq. 2.13 becomes,

$$\frac{\partial^2 E}{\partial x^2} + \frac{\partial^2 E}{\partial y^2} + \frac{\partial^2 E}{\partial z^2} = \mu\epsilon \frac{\partial^2 E}{\partial t^2} \quad \text{V/m}^3 \quad (2.14)$$

The above equation is called Maxwell's EM Wave equation. There are many types of possible EM waves. All these possible EM waves must obey this special wave equation that describes the time and space dependence of the electric field. In an isotropic and linear dielectric medium, the relative permittivity is the same in all directions and is independent of the electric field.

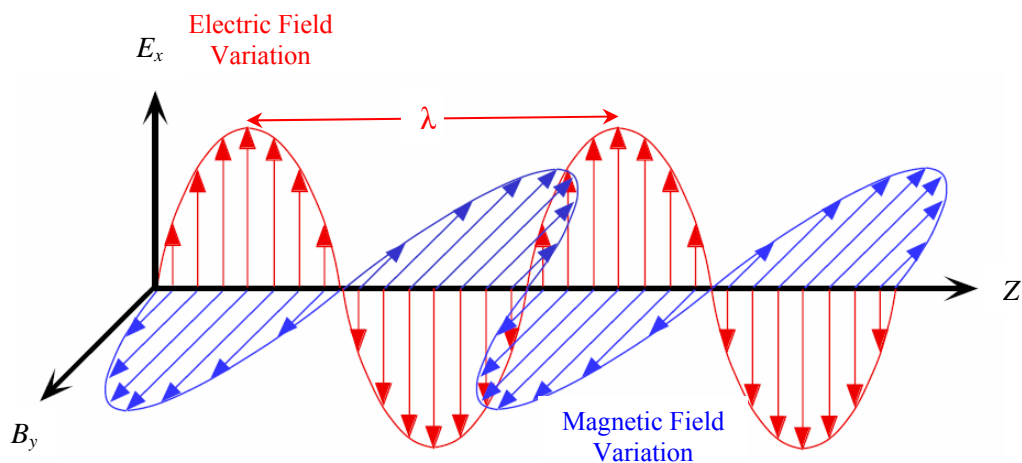
The electric field and the magnetic field are important concepts that can be used to mathematically describe the physical nature of electromagnetic waves such as light. The electric field vibrates transverse (i.e. perpendicular) to the direction the electromagnetic wave is traveling. The magnetic field vibrates in a direction transverse to the direction in which the electromagnetic wave is traveling and transverse to the electric field.

Fig. 2.4 illustrates the behavior of an electromagnetic wave that is polarized along the  $x$ -axis and traveling in the  $z$ -direction. These two fields oscillate in a consistent manner so that the wave moves forward at a constant rate, the speed of light ( $c$ ). Light is an

electromagnetic wave with time varying electric and magnetic fields,  $E_x$  and  $B_y$  respectively, which are propagating in space in such a way that they are always perpendicular to each other. The direction of propagation of the wave is in the  $z$ -direction. Electromagnetic (EM) waves are produced by moving charges. These are changing electric and magnetic fields, carrying energy through space.

EM waves require no medium; they can travel through empty space. Sinusoidal plane waves are one type of electromagnetic waves. Not all EM waves are sinusoidal plane waves, but all EM waves can be viewed as a linear superposition of sinusoidal plane waves traveling in arbitrary directions. A plane EM wave traveling in the  $z$ -direction can be described by,

$$E_x(z, t) = E_o \cos 2\pi (ft - z/\lambda) \quad (2.15)$$



**Fig. 2.4 Spatial Variations of E and H Fields for an EM wave traveling in  $z$ -direction**

Where,  $E_x$  is the electric field at position  $z$  at time  $t$ ,  $k$  is the propagation constant or wave number, which is equivalent to  $(2\pi/\lambda)$ ,  $\lambda$  is the wavelength,  $f$  is the frequency, and  $E_0$  is the amplitude of the wave. The time varying magnetic fields result in time varying electric fields and vice versa. A time varying magnetic field would set up a time varying electric field with the same frequency.

### **2.3.3 Propagation of Electromagnetic Waves**

Electromagnetic waves are the waves which can travel through the vacuum of outer space. Mechanical waves, unlike electromagnetic waves, require the presence of a material medium in order to transport their energy from one location to another. Sound waves are examples of mechanical waves, while light waves are examples of electromagnetic waves. Electromagnetic waves are created by the vibration of an electric charge. This vibration creates a wave which has both an electric and a magnetic component. The propagation of an electromagnetic wave through a material medium occurs at a net speed which is less than  $3 \times 10^8$  m/s.

The mechanism of energy transport through a medium involves the absorption and re-emission of the wave energy by the atoms of the material. When an electromagnetic wave impinges upon the atoms of a material, the energy of that wave is absorbed. The absorption of energy causes the electrons within the atoms to undergo vibrations. After a short period of vibrational motion, the vibrating electrons create a new electromagnetic wave with the same frequency as the first electromagnetic wave. While these vibrations occur for only a very short time, they delay the motion of the wave through the medium.



Once the energy of the electromagnetic wave is re-emitted by an atom, it travels through a small region of space between atoms. Once it reaches the next atom, the electromagnetic wave is absorbed, transformed into electron vibrations and then re-emitted as an electromagnetic wave. While the electromagnetic wave will travel at a speed of 'c' ( $3 \times 10^8$  m/s) through the vacuum of interatomic space, the absorption and re-emission process causes the net speed of the electromagnetic wave to be less than 'c'.

The actual speed of an electromagnetic wave through a material medium is dependent upon the optical density of that medium. When a light passes through a medium, its velocity decreases. For a given frequency of light, the wavelength also must decrease. This decrease in velocity is quantitated by the refractive index,  $n$ , of the medium which is the ratio of  $c$  to the velocity of light in that medium ( $v$ ),  $n = c / v$ . Since the velocity of light is less in media other than in a vacuum,  $n$  is always a number greater than one. Different materials cause different amounts of delay due to the absorption and re-emission process.

Furthermore, different materials have their atoms more closely packed, and thus the distance between atoms is less. These two factors are dependent upon the nature of the material through which the electromagnetic wave is traveling. As a result, the speed of an electromagnetic wave is dependent upon the material through which it is traveling.

## 2.4 Reflection and Transmission of an Electromagnetic Wave

### 2.4.1 Normal Incidence on a Lossless Dielectric

When a uniform plane wave propagating in medium 1 is normally incident on an interface with a second medium with a different dielectric constant as shown in Fig. 2.5, some of the incident wave energy is transmitted into medium 2 and continues to propagate to the right (+z direction). In the following discussion, it is assumed that both media are lossless dielectrics (i.e.,  $\sigma_1, \sigma_2 = 0$ ). Once again, it is assumed that without loss of generality under conditions of normal incidence on a planar boundary, that the incident electric field is oriented in the  $x$ -direction. It is also assumed that the amplitude  $E_0^i$  of the incident wave is real, with no loss of generality, since this basically amounts to the choice of the time origin [1]. The phasor fields for the incident, reflected, and transmitted waves are given as:

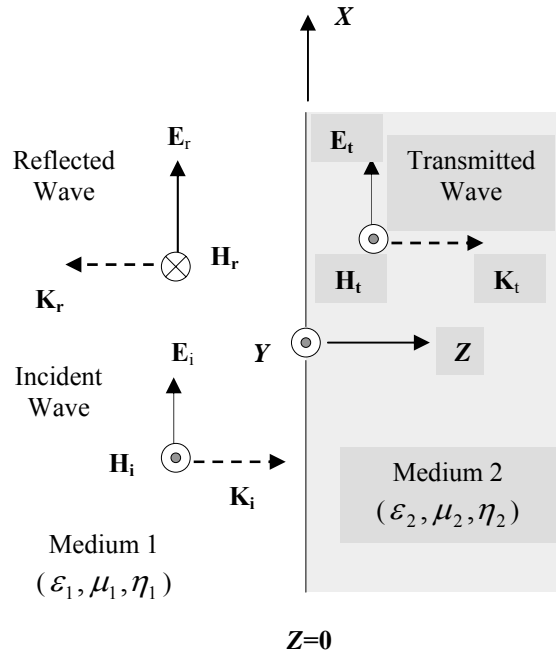


Fig 2.5 Uniform plane wave normally incident on a lossless dielectric boundary

*Incident Wave:*

$$E^i(z) = \hat{x}E_0^i e^{-jk_1 z} \quad (2.16)$$

$$H^i(z) = \hat{y} \frac{E_0^i}{\eta_1} e^{-jk_1 z}$$

*Reflected Wave:*

$$E^r(z) = \hat{x}E_0^r e^{+jk_1 z} \quad (2.17)$$

$$H^r(z) = -\hat{y} \frac{E_0^r}{\eta_1} e^{+jk_1 z}$$

*Transmitted wave*

$$E^t(z) = \hat{x}E_0^t e^{-jk_2 z} \quad (2.18)$$

$$H^t(z) = \hat{y} \frac{E_0^t}{\eta_2} e^{-jk_2 z}$$

Where,  $k_1 = \omega\sqrt{\mu_1\epsilon_1}$ ,  $k_2 = \omega\sqrt{\mu_2\epsilon_2}$  and  $\eta_1 = \sqrt{\mu_1/\epsilon_1}$ ,  $\eta_2 = \sqrt{\mu_2/\epsilon_2}$  are, respectively, the wave number and the intrinsic impedance for medium 1 and medium 2, respectively.

Note that  $E_0^t$  is the amplitude (yet to be determined) of the transmitted wave at  $z=0$ .

From Fig. 2.5 the polarities of  $E^i$  and  $E^r$  have been defined to be the same and  $H^r$  to be in the  $-y$  direction, so that  $E^r \times H^r$  is in the  $-z$  direction. Note that, at this point, the selected orientations of E and H for the different waves (incident, reflected and transmitted) are simply convenient choices. The boundary conditions will determine whether the phasor fields at the boundary are positive or negative according to these assumed conventions.

Assuming the incident wave as given, the next step is to determine the properties of the reflected and transmitted waves so that the fundamental boundary conditions for electromagnetic fields are satisfied at the interface, where all the three waves are related to one another. There are two unknown quantities  $E_0^r$  and  $E_0^t$  to be determined in terms of the incident field amplitude  $E_0^i$ . Two boundary conditions will be used to determine them. The boundary conditions to be employed are 1) the tangential components of the electric field should be continuous across the junction and 2) the tangential components of the magnetic field intensity differ by any surface current that is located at the interface. It is reasonable in practice to assume that this current is equal to zero. This implies that the tangential components of the magnetic field intensity will also be continuous at the interface. Thus, the two boundary conditions are the continuity of the tangential components of both the electric and magnetic fields across the interface. We thus have,

$$E^i(z=0) + E^r(z=0) = E^t(z=0) \Rightarrow E_0^i + E_0^r = E_0^t$$

$$H^i(z=0) + H^r(z=0) = H^t(z=0) \Rightarrow \left( \frac{E_0^i}{\eta_1} - \frac{E_0^r}{\eta_1} \right) = \frac{E_0^t}{\eta_2}$$

The solution of these two equations yields,

$$E_0^r = \frac{\eta_2 - \eta_1}{\eta_2 + \eta_1} E_0^i \quad (2.19)$$

$$E_0^t = \frac{2\eta_2}{\eta_2 + \eta_1} E_0^i \quad (2.20)$$

The reflection and transmission coefficients are defined as follows

$$\Gamma = \frac{E_0^r}{E_0^i} = \frac{\eta_2 - \eta_1}{\eta_2 + \eta_1} \quad (2.21)$$

$$\tau = \frac{E_0^t}{E_0^i} = \frac{2\eta_2}{\eta_2 + \eta_1} \quad (2.22)$$

The quantities  $\Gamma$  and  $\tau$  are called the **Reflection Coefficient** and **Transmission Coefficient**, respectively. For lossless dielectric media,  $\eta_1$  and  $\eta_2$  are real quantities; consequently, both  $\Gamma$  and  $\tau$  are real also. Note that, physically, the above coefficients are derived from the application of the boundary conditions, which are valid for all media in general. Complex reflection and transmission coefficients may result when  $\eta_2$  and/or  $\eta_1$  are complex (i.e., one or both of the media are lossy), meaning that in addition to the differences in amplitudes, phase shifts are also introduced between the incident, reflected and transmitted fields at the interface. From Eqs. (2.21) and (2.22) it can be easily shown that  $\Gamma$  and  $\tau$  are interrelated by the simple formula,

$$\tau = 1 + \Gamma \quad (2.23)$$

For nonmagnetic media,

$$\begin{aligned} \eta_1 &= \frac{\eta_0}{\sqrt{\epsilon_{r_1}}}, \\ \eta_2 &= \frac{\eta_0}{\sqrt{\epsilon_{r_2}}}, \end{aligned} \quad (2.24)$$

Where,  $\eta_0$  is the intrinsic impedance of free space, in which case Eqs. (2.21) and (2.22) may be written as,

$$\Gamma = \frac{\sqrt{\epsilon_{r_1}} - \sqrt{\epsilon_{r_2}}}{\sqrt{\epsilon_{r_1}} + \sqrt{\epsilon_{r_2}}} \quad (2.25)$$

$$\tau = \frac{2\sqrt{\epsilon_{r_1}}}{\sqrt{\epsilon_{r_1}} + \sqrt{\epsilon_{r_2}}} \quad (2.26)$$

For most dielectrics and insulators, the magnetic permeability does not differ appreciably from the free space value. Hence,  $\mu_1 = \mu_2 = \mu_0$  and since the characteristic impedance,  $Z = \sqrt{\mu/\epsilon}$ . Eqs. (2.25) and (2.26) can be written as,

$$\Gamma = \frac{\sqrt{Z_2} - \sqrt{Z_1}}{\sqrt{Z_2} + \sqrt{Z_1}} \quad (2.27)$$

$$\tau = \frac{2\sqrt{Z_2}}{\sqrt{Z_2} + \sqrt{Z_1}} \quad (2.28)$$

Hence, knowing the characteristic impedance of the materials allows one to determine the propagation characteristics and amplitudes of the wave that is transmitted into the second material and of the wave that is reflected at the interface and propagates back into the first material. If the characteristic impedances on both sides of the interface are equal, all of the incident electromagnetic energy will be transmitted into region 2 and none reflected back into region 1. This is called matching the media, which has many practical applications.

### 2.4.2 Oblique Incidence at a Dielectric Boundary

For normal incidence, the reflection coefficient  $\Gamma$  and transmission coefficient  $\tau$  of a boundary between two different media is independent of the polarization of the incident

wave, because the electric and magnetic fields of a normally incident plane wave are both always tangential to the boundary regardless of the wave polarization. This is not the case for oblique incidence at an angle  $\theta_i \neq 0$ . A wave with any specified polarization may be described as the superposition of two orthogonally polarized waves, one with its electric field parallel to the plane of incidence (parallel polarization) and another with its electric field perpendicular to the plane of incidence (perpendicular polarization) [1]. These two kinds of polarizations will now be briefly discussed.

#### 2.4.2.1 Perpendicular Polarization

The expressions for the wave electric and magnetic field phasors of the incident, reflected, and refracted (transmitted) waves shown in Fig. 2.6 can be expressed as

*Incident Wave:*

$$E^i(x, z) = \hat{y}E_0^i e^{-jk_1(x \sin \theta_i + z \cos \theta_i)} \quad (2.29)$$

$$H^i(x, z) = \frac{E_0^i}{\eta_1} (-\hat{x} \cos \theta_i + \hat{z} \sin \theta_i) e^{-jk_1(x \sin \theta_i + z \cos \theta_i)}$$

*Reflected Wave:*

$$E^r(x, z) = \hat{y}E_0^r e^{-jk_1(x \sin \theta_r - z \cos \theta_r)} \quad (2.30)$$

$$H^r(x, z) = \frac{E_0^r}{\eta_1} (\hat{x} \cos \theta_r + \hat{z} \sin \theta_r) e^{-jk_1(x \sin \theta_r - z \cos \theta_r)}$$

*Transmitted wave*

$$E^t(x, z) = \hat{y}E_0^t e^{-jk_2(x \sin \theta_t + z \cos \theta_t)} \quad (2.31)$$

$$H^t(x, z) = \frac{E_0^t}{\eta_2} (-x \cos \theta_t + \hat{z} \sin \theta_t) e^{-jk_2(x \sin \theta_t + z \cos \theta_t)}$$

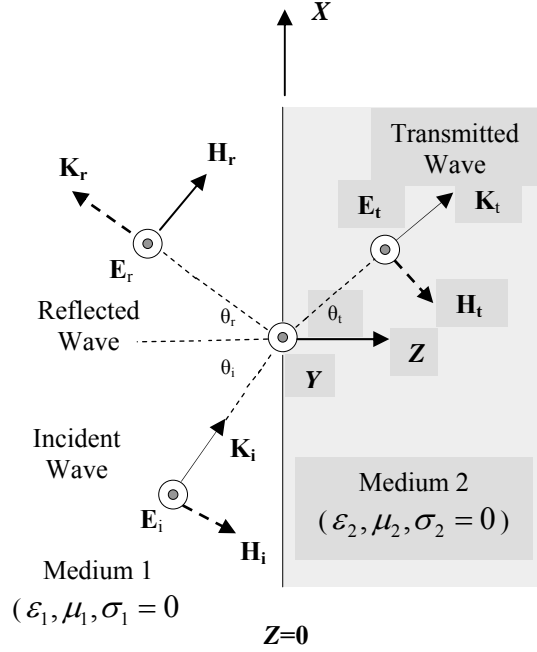


**Fig. 2.6 A perpendicularly polarized wave incident on a dielectric boundary**

To determine the amplitudes of the reflected and transmitted wave fields in terms of the incident field amplitude  $E_0^i$ , one can apply the boundary condition concerning the continuity of the tangential component of the wave electric field across the interface. Considering the field orientations as defined in Fig. 2.6, then, at  $z = 0$ ,

$$E_0^i e^{-jk_1 x \sin \theta_i} + E_0^r e^{-jk_1 x \sin \theta_r} = E_0^t e^{-jk_2 x \sin \theta_t} \quad (2.32)$$

Since this condition has to be satisfied for all values of  $x$ , all three components must be equal. Thus,

$$k_1 x \sin \theta_i = k_1 x \sin \theta_r = k_2 x \sin \theta_t \quad (2.33)$$

The first equality in (2.33) leads to



$$\theta_i = \theta_r \quad (2.34)$$

Eq (2.34) is commonly referred to as ***Snell's law***. The second equality in (2.33) leads to

$$\frac{\sin \theta_i}{\sin \theta_t} = \frac{k_2}{k_1} = \frac{\omega \sqrt{\mu_2 \epsilon_2}}{\omega \sqrt{\mu_1 \epsilon_1}} = \frac{n_2}{n_1} \quad (2.35)$$

Eq. (2.35) is commonly referred to as Snell's law of refraction. Rewriting the boundary condition at any given value of x, (say at x=0)

$$E_0^i + E_0^r = E_0^t \Rightarrow \frac{E_0^t}{E_0^i} = 1 + \frac{E_0^r}{E_0^i} \quad (2.36)$$

On the basis of the conservation of power we must have,

$$|S_{av}|_i \cos \theta_i = |S_{av}|_r \cos \theta_r + |S_{av}|_t \cos \theta_t \quad (2.37)$$

$$\frac{1}{2\eta_1} E_0^{i^2} \cos \theta_i = \frac{1}{2\eta_1} E_0^{r^2} \cos \theta_r + \frac{1}{2\eta_2} E_0^{t^2} \cos \theta_t$$

or

$$\frac{E_0^{r^2}}{E_0^{i^2}} = 1 - \frac{\eta_1 E_0^{t^2} \cos \theta_t}{\eta_1 E_0^{i^2} \cos \theta_i} \quad (2.38)$$

Now substituting Eq. (2.36) into Eq. (2.38) and manipulating the result to solve for  $\frac{E_0^r}{E_0^i}$

(by eliminating  $E_0^t$ ), the result is,

$$\Gamma_{\perp} = \frac{E_0^r}{E_0^i} = \frac{\eta_2 \cos \theta_i - \eta_1 \cos \theta_t}{\eta_2 \cos \theta_i + \eta_1 \cos \theta_t} \quad (2.39)$$

Where,  $\Gamma_{\perp}$  is called the reflection coefficient for perpendicular polarization. For magnetically identical media ( $\mu_1 = \mu_2$ ), and using Eq. (2.35), one can obtain the alternate expression for  $\Gamma_{\perp}$ ,

$$\Gamma_{\perp} = \frac{E_0^r}{E_0^i} = \frac{\cos \theta_i - \sqrt{\epsilon_{r_2} / \epsilon_{r_1}} \cos \theta_t}{\cos \theta_i + \sqrt{\epsilon_{r_2} / \epsilon_{r_1}} \cos \theta_t} = \frac{\cos \theta_i - \sqrt{(\epsilon_{r_2} / \epsilon_{r_1}) - \sin^2 \theta_i}}{\cos \theta_i + \sqrt{(\epsilon_{r_2} / \epsilon_{r_1}) - \sin^2 \theta_i}} \quad (2.40)$$

The transmission coefficient  $\tau_{\perp}$  can be found from Eqs. (2.38) and (2.39) as

$$\tau_{\perp} = \frac{E_0^t}{E_0^i} = \frac{2\eta_2 \cos \theta_i}{\eta_2 \cos \theta_i + \eta_1 \cos \theta_t} \quad (2.41)$$

For magnetically identical media ( $\mu_1 = \mu_2$ ), Eq. (2.41) becomes,

$$\tau_{\perp} = \frac{2 \cos \theta_i}{\cos \theta_i + \sqrt{\epsilon_{r_2} / \epsilon_{r_1}} \cos \theta_t} = \frac{2 \cos \theta_i}{\cos \theta_i + \sqrt{\epsilon_{r_2} / \epsilon_{r_1} - \sin^2 \theta_i}} \quad (2.42)$$

Hence,

$$1 + \Gamma_{\perp} = \tau_{\perp} \quad (2.43)$$

### 2.4.2.2 Parallel Polarization

The expressions for the wave electric and magnetic field phasors of the incident, reflected, and refracted (transmitted) waves shown in Fig. 2.7 can be expressed as

*Incident Wave:*

$$E^i(x, z) = E_0^i(\hat{x} \cos \theta_i - \hat{z} \sin \theta_i) e^{-jk_1(x \sin \theta_i + z \cos \theta_i)} \quad (2.44)$$

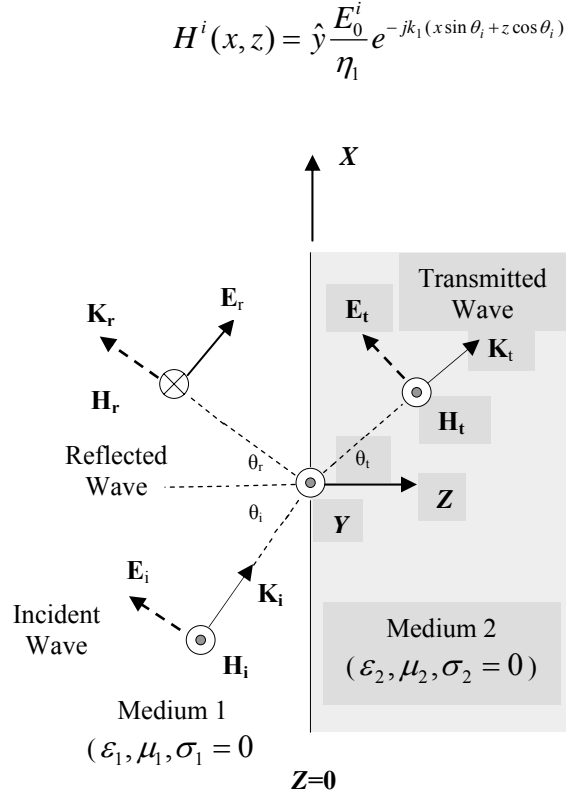


**Fig 2.7 A parallel polarized wave at a dielectric boundary**

*Reflected Wave:*

$$E^r(x, z) = E_0^r(\hat{x} \cos \theta_r + \hat{z} \sin \theta_r) e^{-jk_1(x \sin \theta_r - z \cos \theta_r)} \quad (2.45)$$

$$H^r(x, z) = -\hat{y} \frac{E_0^r}{\eta_1} e^{-jk_1(x \sin \theta_r - z \cos \theta_r)}$$

*Transmitted wave*

$$E^t(x, z) = E_0^t(\hat{x} \cos \theta_t - \hat{z} \sin \theta_t) e^{-jk_2(x \sin \theta_t + z \cos \theta_t)} \quad (2.46)$$

$$H^t(x, z) = \hat{y} \frac{E_0^t}{\eta_2} e^{-jk_2(x \sin \theta_t + z \cos \theta_t)}$$

Following a procedure similar to that used for the perpendicular polarization case to find the amplitudes of the reflected and transmitted waves in terms of  $E_0^i$ , apply the boundary

condition concerning the continuity of the tangential component of the wave electric field across the interface. Therefore, at  $z = 0$ ,

$$(E_0^i + E_0^r) \cos \theta_i = E_0^t \cos \theta_t$$

or

$$\frac{E_0^t}{E_0^i} = \left( 1 + \frac{E_0^r}{E_0^i} \right) \frac{\cos \theta_i}{\cos \theta_t} \quad (2.47)$$

Substituting Eq. (2.47) into Eq. (2.38) and manipulating the result to solve for  $E_0^r / E_0^i$  (by eliminating  $E_0^t$ ), the result is,

$$\Gamma_{\parallel} = \frac{E_0^r}{E_0^i} = \frac{-\eta_1 \cos \theta_i + \eta_2 \cos \theta_t}{\eta_1 \cos \theta_i + \eta_2 \cos \theta_t} \quad (2.48)$$

For magnetically identical media ( $\mu_1 = \mu_2$ ),

$$\Gamma_{\parallel} = \frac{\cos \theta_t - \sqrt{\varepsilon_2 / \varepsilon_1} \cos \theta_i}{\cos \theta_t + \sqrt{\varepsilon_2 / \varepsilon_1} \cos \theta_i} = \frac{-\cos \theta_i + (\varepsilon_{r_1} / \varepsilon_{r_2}) \sqrt{(\varepsilon_{r_2} / \varepsilon_{r_1}) - \sin^2 \theta_i}}{\cos \theta_i + (\varepsilon_{r_1} / \varepsilon_{r_2}) \sqrt{(\varepsilon_{r_2} / \varepsilon_{r_1}) - \sin^2 \theta_i}} \quad (2.49)$$

which is the reflection coefficient for parallel polarization, then eliminating  $E_0^r$  we find,

$$\tau_{\parallel} = \frac{E_0^t}{E_0^i} = \frac{2\eta_2 \cos \theta_i}{\eta_1 \cos \theta_i + \eta_2 \cos \theta_t} \quad (2.50)$$

For magnetically identical media ( $\mu_1 = \mu_2$ ),

$$\tau_{\parallel} = \frac{2 \cos \theta_i}{\cos \theta_t + \sqrt{\varepsilon_{r_2} / \varepsilon_{r_1}} \cos \theta_i} = \frac{2 \sqrt{\varepsilon_{r_1} / \varepsilon_{r_2}} \cos \theta_i}{\cos \theta_i + \sqrt{\varepsilon_{r_1} / \varepsilon_{r_2}} \sqrt{1 - (\varepsilon_{r_1} / \varepsilon_{r_2}) \sin^2 \theta_i}} \quad (2.51)$$

From Eqs. (2.49) and (2.51) it is noted that,

$$1 + \Gamma_{\parallel} = \tau_{\parallel} \left( \frac{\cos \theta_t}{\cos \theta_i} \right)$$

These wave propagation concepts can be applied for the analysis of an MSM photodetector as the EM wave incident on the gratings of the photodetector reaches the device active region.

## 2.5 Energy Transported by the EM Waves

Electromagnetic waves transport energy through space. In free space, this energy is transported by the wave with speed  $c$ . The magnitude of the energy flux,  $S$ , is the amount of energy that crosses a unit area perpendicular to the direction of propagation of the wave per unit time. It is given by

$$S = E \times H / (\mu_0) \quad (2.52)$$

Since, for electromagnetic waves  $H = E / c$ ,  $\mu_0$  is a constant called the permeability of free space,  $\mu_0 = 4\pi \times 10^{-7} H / m$ . The **Poynting vector** is the energy flux vector. Its direction is the direction of propagation of the wave, i.e. the direction in which the energy is transported.

$$S = (1 / \mu_0) E \times H \quad (2.53)$$

Energy per unit area per unit time is power per unit area.  $S$  represents the power per unit area in an electromagnetic wave. If an electromagnetic wave falls onto an area  $A$  where it is absorbed, then the power delivered to that area is

$$P = \int_A \langle S \rangle \cdot dA = S \cdot A \quad (2.54)$$

This concept of the transmission of energy can be applied for an MSM photodetector as the wave, after propagating in the Si grating region, reaches the active region of the detector. Eq. (2.54) will be used in later chapters for analyzing the variations in the amplitude of the electric field intensity of an MSM photodetector with and without gratings.

## **CHAPTER 3**

### **LITERATURE REVIEW**

Photodetectors are semiconductor devices that can detect optical signals through electronic processes. The extension of coherent and incoherent light sources into the far-infrared region on one hand, and the ultraviolet region on the other, has increased the need for high speed, sensitive photodetectors.

High speed and high-sensitivity photodetectors have been studied extensively in the past ten years [2], owing to their application in broad-band optical communication network and optical generation of high-power microwave/millimeter waves [3]. R. G. DeCorby et al. [4] developed techniques to improve the speed and efficiency of the photodetectors. In this paper they discussed how photodetectors are generally designed with a balance of bandwidth, efficiency, and power-handling considerations that are to be used in telecommunications and optoelectronics.

The Metal-Semiconductor-Metal photodetector (MSM PD), which is a special kind of photodetector, was proposed and demonstrated by Sugeta et al. in 1979 [5]. MSM PD's have excellent potential as high-performance components for high-speed light wave communication systems and optoelectronic integrated circuits due to their low capacitance per unit area and their high speed. MSM PD's deserve special attention due to their high electrical bandwidth and ability to generate ultrashort electrical pulses [6].

Metal-silicon-metal cladding layers exhibit coupling and absorption characteristics which make them useful as photodetectors for integrated optical applications.

In the past few years MSM PD's have become very popular in the field of optical communications because of their numerous advantages [3], [7]. One of the most important properties of this type of detector is its high response speed, determined by the geometry of the structure and by the low capacity of the detector. The other most important property is the efficiency of the MSM photodetector. The basic aim in further development of MSM PD's is to achieve an improvement of these properties. There is therefore an increasing interest in the modeling of MSM PD's and the computer simulation of their response. Although this device has a high bandwidth, it suffers from relatively low quantum efficiency due to high metal–reflection loss.

Both Si and GaAs metal-semiconductor-metal (MSM) photodetectors are viable candidates for monolithically integrated optical receivers in fiber optic communications and as free space interconnects [8]. GaAs is more attractive due to its short absorption length ( $\sim 1.0 \mu\text{m}$  at  $\lambda = 850 \text{ nm}$ ), making it possible to combine large bandwidth with good responsivity [9]. These detectors operate at very high frequencies (UV and visible spectral range). Si offers the potential of lower cost; direct integration with VLSI optoelectronic circuits with good sensitivity, but poor response times have been reported [10].



Silicon MSM photodetectors have been used since 1960. The use of these silicon photodetectors is continually growing in various fields of science such as astronomy, medicine, material testing, etc. More recently, with the fast development of biotechnology, the need for a photodetector that works in the UV range with high responsivity has become clear. M. Caria et al. [11] demonstrated that commercial silicon photodetectors have a high responsivity in the UV range (200-400 nm). In the UV range of interest, the absorption length in silicon is approximately 50–800 Å. They have investigated the properties of different types of commercial silicon photodetectors including pixel and microstrip devices with different bulk and surface composition from different vendors.

Liu et al. [12] have reported improved response speed by fabricating MSM photodetectors on Si-on-insulator (SOI) substrates. The key feature in speed enhancement is the buried oxide layer that limits the active Si thickness. By reducing the Si film thickness to 100 nm, a photo detector bandwidth of 140 GHz at a 780-nm wavelength was achieved, however, at the cost of very low quantum efficiency.

Lee et al. [13] have proposed a MSM detector configuration on a 5- $\mu\text{m}$  thick Si membrane, where the trapping of light in a thin membrane results in minimal reduction in responsivity, while reducing carrier transit times. Other attempts to improve the absorption of Si by hydrogenated amorphous Si (a-Si:H) have focused on modifying the long-range structural symmetry of crystalline Si by relaxing the k-selection rule for optical transition [14].

Over the past few years' interest has grown in the interdigitated MSM detector due to its ease of integration with IC processes, its very low capacitance, and its high speed. Using this type of detector, optical communication receivers have been fabricated on integrated circuits. Interdigitated finger MSM detectors have been used widely as high-speed photodetectors and have also been used as (OE) optoelectronic mixers to generate radio-frequency sub-carriers in fiber optic microwave links [15]. Recently, an MSM detector has been utilized as an OE mixer in a frequency modulated continuous-wave laser detection and ranging (LADAR) system [16].

The response speed of the MSM-PD is largely limited by the transit time of the photogenerated carriers, and thus the inter-electrode spacing should be small. As the fabrication technology advances, the finger spacing of the MSM-PD decreases down to the sub-micrometer and even nanometer scale. MSM-PD's with only 25 nm finger width and spacing were fabricated using e-beam lithography [17]. When the finger spacing of a MSM photodetector is smaller than the wavelength of light, the transmission of TE and TM waves through the detector fingers becomes strongly dependent on the wavelength and polarization of the incident light.

For optimum performance of the MSM photodetector, the amount of energy reaching the interface of the detector should be maximum, which also depends on the geometric and optical parameters of the structures as well as on the properties of the incident radiation (wavelength, polarization, angle of incidence etc.). J.J. Kuta et al [18] demonstrated how polarization and wavelength account for the response of a MSM photodetector. For

structures which are large compared to the wavelength, sufficiently good approximations can be obtained by means of simple geometrical optics models. As feature sizes become smaller, the errors caused by neglecting diffraction and interference effects increase. When the feature sizes are below the order of a few wavelengths, rigorous electromagnetic models are necessary to obtain reasonably accurate results.

It was found from [19] that approximately 30% of the incident light is reflected at the interface between the air and the detector surface. If one neglects the grating effect of fine metal fingers, these effects, in combination with occultation of the possible absorbing surface area by the metal electrodes of, typically, at least 25%, can reduce the overall quantum efficiency to much less than 25%.

A special kind of detector called the Resonant Cavity Enhanced (RCE) photodetector, having high quantum efficiency was demonstrated by Kishino et al. [20]. This is achieved by utilizing reflectors around the active region. The photons make multiple passes across the active region, improving the probability of absorption, thereby increasing the quantum efficiency. Some attempts have been aimed at improving the Si MSM detector quantum efficiency at visible and near IR wavelengths by fabricating vertical and U-shaped trench electrodes using reactive ion etching and wet chemical etching methods [21], [22].

A. K. Sharma [23] proposed a technique to improve the efficiency of the MSM Photodetector. A simple ion implantation step was used on a Ni-Si-Ni metal-

semiconductor-metal photodetector to create a highly absorbing region ( $\sim 1 \mu\text{m}$ ) below the Si surface, whereby, the internal quantum efficiency was improved by a factor of  $\sim 3$  at 860 nm (up to 64 %) and a full factor of ten at  $1.06 \mu\text{m}$  (up to 23 %) as compared with otherwise identical non-implanted devices.

S. H. Zaidi and A. K. Sharma [24] demonstrated the performance of a Si MSM photodetector incorporating one-dimensional (1-D) arrays of rectangular (wall) and triangular-shaped nanoscale structures within their active regions. It has been shown that these gratings account for higher transmission of energy, thereby increasing the charge collection efficiency.

A new technique was proposed by Stéphane Collin et al. [25] for efficient light absorption in MSM photodetectors. It was shown that the confinement of light in sub wavelength metal–semiconductor gratings can be achieved by Fabry–Pérot resonances involving vertical transverse magnetic and transverse electric guided waves, thereby increasing the quantum efficiency.

Recently, Sang-Woo Seo et al. [26] demonstrated a new kind of MSM photodetector called an inverted metal semiconductor metal (IMSM) photodetector that has higher efficiency. These are thin film MSM's without the growth substrate. IMSM's have fingers at the bottom of the device to enhance the efficiency.

In this thesis, it is shown that having a wall-like Si grating on the active region of the detector increases the charge collection efficiency and rearranging the wall lattice to a square lattice could improve the collection efficiency further. It has been demonstrated how these structural changes at the interface accounts for higher transmitted energy and the subsequent generation and collection of carriers at the interface, thus contributing to enhanced collection efficiency. Variations in the electric field intensity due to the change in the number and the dimensions of square gratings are also demonstrated. It is also shown that cladding the detector gratings increases the concentration efficiency of the photodetector.

## **CHAPTER 4**

### **THE SIMULATION METHOD**

#### **4.1 Introduction**

The previous chapter gave an idea about the previous research work done on MSM Photodetectors. It discussed the various attempts to increase the efficiency of the photodetector. This chapter outlines the different numerical techniques used to solve the complicated electromagnetic problems, followed by the basic concepts of the Finite Integration Technique (FIT). It concludes with a brief introduction to the simulation software used in the current analysis.

Numerical techniques are extremely useful in solving real-life problems with complex materials and geometries. There are a variety of electromagnetic modeling techniques. For solving complicated electromagnetic scattering problems, there are three main numerical techniques. First is the Finite Difference Time Domain (FDTD) technique, which was first proposed by Yee in 1966 [27]. This technique is a computational method that calculates the temporal evolution of the electromagnetic field within a region of space by stepping through time. At each time step, centered finite difference approximations are used to calculate the space and time differences on a Cartesian grid. The electric and the magnetic fields are defined by six field components, which all lie on a different point on the grid, especially defined to fit into the FDTD scheme. This leads to an explicit time stepping algorithm which is of second order accuracy in both time and space.

The category of calculations can be subdivided into steady state and transient analysis. In the steady state analysis, the excitation is harmonic. Time stepping is carried out until steady state is reached, i.e. all transients have vanished. The excitation used for the transient analysis can have any time function. It may be an incident plane wave or an impressed voltage or current at discrete points. The result is a function of time, which is transformed to the frequency domain with a special FFT to obtain the frequency response of the system.

Local methods such as the FDTD method are by necessity formulated as initial value problems on a finite portion of space (the computational domain). As such, the solution of scattering and radiation problems requires a mechanism to enforce the radiation condition which prescribes the behavior of the electromagnetic fields at infinity. This is achieved by applying second-order absorbing boundary conditions which truncate the FDTD space grid and compensate for reflections on the boundary of the problem space.

The second method is the Electric Field Integral Equation (EFIE) method. The scattering of arbitrarily-shaped perfectly-conducting bodies is solved using a surface integral equation formulation for the electric field. The electric field (surface) integral equation is solved by using the method of moments in which the testing functions of the electric field and the expansion functions of the electric surface current density are both appropriate triangular-patch functions. The system of equations is then solved by using a LU factorization algorithm.

EFIE method is applicable to both open and closed surfaces. However, the EFIE fails near internal resonances of a closed body. Several methods are available for eliminating this difficulty, but all involve significant additional computation. Another difficulty is that the EFIE solution procedure becomes unstable when the dimensions of the scatterer become very small with respect to the wavelength of the incident field. The principal modification to the original EFIE code includes the use of a new matrix factorization routine, which results in a significant reduction in computer time.

The third technique is the Finite Integration Technique (FIT). This technique is discussed in detail in the following section, and this method has been used for all the simulations in this thesis.

## **4.2 The Finite Integration Technique (FIT)**

The Finite Integration Technique (FIT), was first proposed by Weiland in 1976/77 [28]. This numerical method provides a universal spatial discretization scheme, applicable to various electromagnetic problems, ranging from static field calculations to high frequency applications in the time or frequency domain. In the following section, the main aspects of this procedure will be explained and afterwards extended to specialized forms concerning the different solver types. Unlike most numerical methods, the FIT discretizes the following *integral* form of Maxwell's equations, rather than the differential one:



$$\oint_{\partial A} \vec{E} \cdot d\vec{s} = - \int_A \frac{\partial \vec{B}}{\partial t} \cdot d\vec{A}, \quad (4.1)$$

$$\oint_{\partial A} \vec{H} \cdot d\vec{s} = \int_A \left( \frac{\partial \vec{D}}{\partial t} + \vec{J} \right) \cdot d\vec{A}$$

$$\oint_{\partial V} \vec{D} \cdot d\vec{A} = \int_V \rho \cdot dV$$

$$\oint_{\partial V} \vec{B} \cdot d\vec{A} = 0 \quad (4.2)$$

In order to solve these equations numerically, a finite calculation domain is defined, enclosing the considered application problem. By creating a suitable mesh system, this domain is split up into several small cuboids, so-called grid cells. This first or primary mesh can be visualized in CST Microwave Studio [29] in the *Mesh View*; however, internally a *second* or *dual mesh* is set up orthogonally to the first one. The Spatial discretization of Maxwell's equations is finally performed on these two orthogonally grid

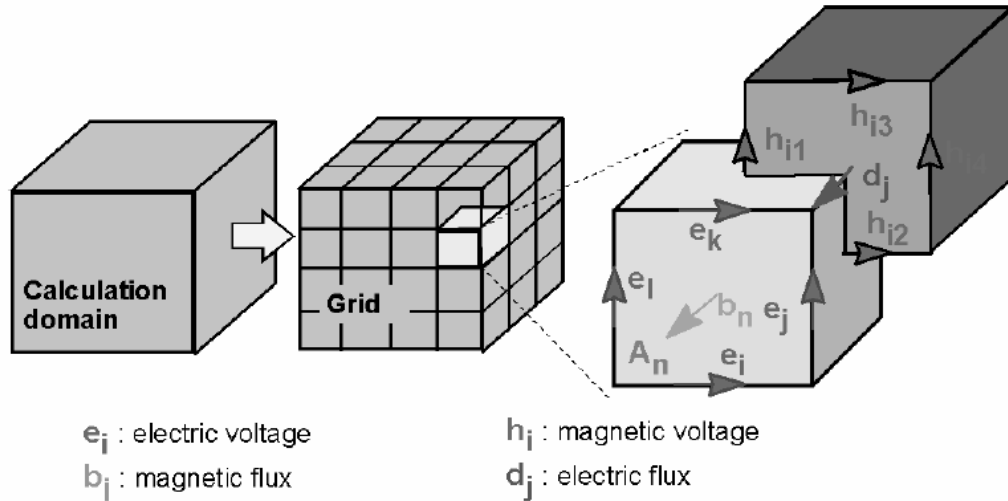


Figure 4.1 Allocation of the grid voltages and facet fluxes on the primary and dual grids

systems, where the new degrees of freedom are introduced as integral values as well. The electric grid voltages  $\mathbf{e}$  and magnetic facet fluxes  $\mathbf{b}$  are allocated on the primary grid  $\mathbf{G}$  and the dielectric facet fluxes  $\mathbf{d}$  as well as the magnetic grid voltages  $\mathbf{h}$  on the dual grid  $\tilde{\mathbf{G}}$  (indicated by the tilde) as shown in Fig 4.1.

Now, Maxwell's equations are formulated for each of the cell facets separately as will be demonstrated in the following. Considering Faraday's law, the closed integral on the left side of Eq. (4.1) can be rewritten as a sum of four grid voltages without introducing any supplementary errors. Consequently, the time derivative of the magnetic flux defined on the enclosed primary cell facet represents the right-hand side of the Eq. (4.1), as illustrated in Figure 4.2 below. By repeating this procedure for all available cell facets, the calculation rule can be summarized in an elegant matrix formulation, introducing the topological matrix  $\mathbf{C}$  as the discrete equivalent of the analytical curl operator. Applying this scheme to Ampere's law on the dual grid involves the definition of a corresponding discrete curl operator  $\tilde{\mathbf{C}}$ .

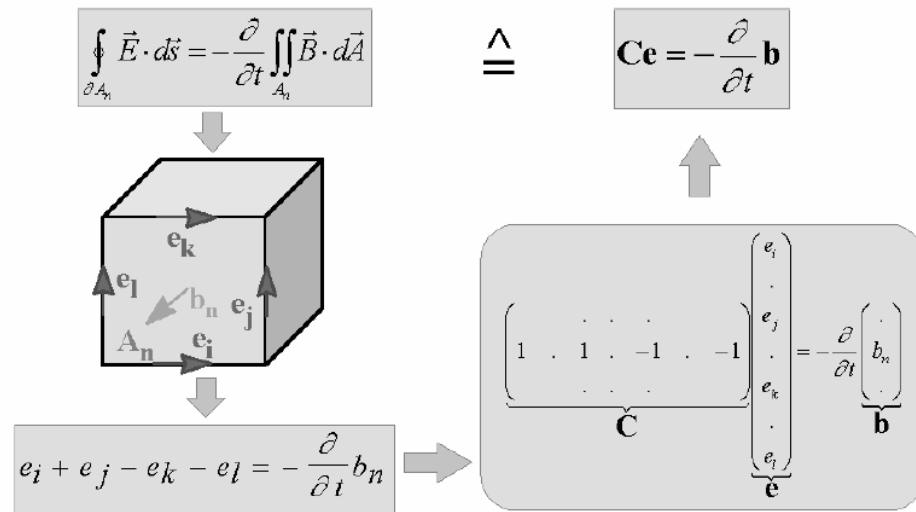


Figure 4.2 Time derivative of the magnetic flux defined on the enclosed primary cell facet

Similarly, the discretization of the remaining divergence equations (Eq. (4.2)) introduces discrete divergence operators  $S$  and  $\tilde{S}$ , belonging to the primary and dual grid, respectively. As previously indicated, these discrete matrix operators just consist of elements '0', '1' and '-1', representing merely topological information. Finally, the complete discretized set of the so-called *Maxwell's Grid Equations* (MGE's) is obtained.

$$\begin{aligned} Ce &= -\frac{d}{dt}b \\ \tilde{C}h &= \frac{d}{dt}d + j \end{aligned} \tag{4.3}$$

$$\begin{aligned} \tilde{S}d &= q \\ Sb &= 0 \end{aligned} \tag{4.4}$$

Compared to the continuous form of Maxwell's equations, the similarity between both descriptions is obvious. Once again, it should be mentioned that no additional error has yet been introduced. This essential point of the FIT discretization process is reflected in the fact that important properties of the continuous gradient, curl and divergence operators are still maintained in grid space:

$$SC = \tilde{S}\tilde{C} = 0 \quad \Leftrightarrow \quad \text{div rot} \equiv 0 \tag{4.5}$$

$$C\tilde{S}^T = \tilde{C}S^T = 0 \quad \Leftrightarrow \quad \text{rot grad} \equiv 0 \tag{4.6}$$

At this point, it should be mentioned that even the spatial discretization of a numerical algorithm could cause long term instability. However, based on the presented fundamental relations (Eqs. 4.5 and 4.6), it can be shown that the FIT formulation is not affected by such problems, since the set of MGE's (Eqs. 4.3 and 4.4) maintain energy and charge conservation [30].

Finally, the missing material equations introduce the inevitable numerical inaccuracy due to the spatial discretization. By defining the necessary relations between voltages and fluxes, their integral values have to be approximated over the grid edges and cell areas, respectively. Consequently, the resulting coefficients depend on the averaged material parameters as well as on the spatial resolution of the grid and are summarized again in correspondent matrices as follows:

$$\vec{D} = \varepsilon \vec{E} \quad \Rightarrow \quad d = M_\varepsilon e \quad (4.7)$$

$$\vec{B} = \mu \vec{H} \quad \Rightarrow \quad b = M_\mu h \quad (4.8)$$

$$\vec{J} = \sigma \vec{E} + \vec{J}_s \quad j = M_\sigma e + j_s \quad (4.9)$$

Now, all matrix equations are available to solve electromagnetic field problems on the discrete grid space. The fact that the topological and metric information are divided into different equations has important theoretical, numerical and algorithmic consequences [30]. Therefore, the FIT formulation is a very general method and can be applied to all frequency ranges, from DC to high frequencies.

### 4.3 Implementation of FIT Equations into Simulation Software

The simulation method used for the analysis is based on Finite Integration Technique capable of analyzing broadband structures, specifically in the high-frequency range. CST Microwave Studio is a fully featured software package for electromagnetic analysis and design in the high frequency range [29]. It simplifies the process of inputting the structure by providing a powerful solid modeling front-end which is based on the ACIS modeling kernel. Strong graphic feedback simplifies the definition of your device even further.

After the component has been modeled, a fully automatic meshing procedure (based on an expert system) is applied before the simulation engine is started. The simulators feature the Perfect Boundary Approximation (PBA method) and its Thin Sheet Technique (TST) extension, which increases the accuracy of the simulation by an order of magnitude in comparison to conventional simulators. Since no method works equally well in all application domains, the software contains four different simulation techniques (transient solver, frequency domain solver, eigenmode solver, and modal analysis solver) which best fit their particular applications.

#### **4.3.1 Transient Solver**

The most flexible tool is the transient solver, which can obtain the entire broadband frequency behavior of the simulated device from only one calculation run (in contrast to the frequency stepping approach of many other simulators). This solver is very efficient for most kinds of high frequency applications, such as connectors, transmission lines, filters, antennas and many more. A very important feature of the transient solver is the excellent linear scaling of the computational resources with structure size. Currently, modern personal computers allow the simulation of structures with a size of up to roughly 100 wavelengths. This simulator is equipped with the new Multilevel Subgridding Scheme (MSS), which helps to improve the meshing efficiency and thus, can significantly speed up simulations, especially for complex devices. This solver is used for all the simulations performed in this thesis. These are some of the important features of the Transient Solver:

- Efficient calculation for loss-free and lossy structures
- Broadband calculation of S-parameters from one single calculation run by applying DFT's to time signals
- Calculations of field distributions as a function of time or at multiple selected frequencies from one simulation run
- Adaptive mesh refinement in 3D
- Plane wave excitation (linear, circular or elliptical polarization)
- S-parameter symmetry option to decrease solve time for many structures
- Calculation of various electromagnetic quantities such as: Electric fields, magnetic fields, surface currents, power flows, current densities, power loss densities, electric energy densities, magnetic energy densities, voltages in time and frequency domain
- Antenna farfield calculation (including gain, beam direction, side lobe suppression, etc.) with and without farfield approximation. Farfield probes to determine broad band farfield data at certain angles
- Simultaneous port excitation with different excitation signals for each port

### **4.3.2 Eigenmode Solver**

However, an efficient filter design often requires the direct calculation of the operating modes in the filter rather than an S-parameter simulation. For these cases, CST Microwave Studio also features an eigenmode solver which efficiently calculates a finite number of modes in closed electromagnetic devices. When investigating highly resonant structures such as narrow bandwidth filters, a time domain approach may become

inefficient, because of the slowly decaying time signals. The usage of advanced signal processing techniques (AR-filters) provided by CST Microwave Studio allows the speeding up of these simulations by orders of magnitude compared to standard time domain methods. These are the important features of the Eigenmode Solver.

- Calculation of modal field distributions in closed loss free or lossy structures
- Adaptive mesh refinement in 3D
- Calculation of losses and Q-factors for each mode (direct or by using a perturbation method)
- Automatic parameter studies using the built in parameter sweep tool
- Automatic structure optimization for arbitrary goals using the built-in optimizer

### **4.3.3 Modal Analysis Solver**

Furthermore, CST Microwave Studio also contains a so-called modal analysis solver which works in combination with the eigenmode solver. After the modes of a filter have been calculated, this very efficient technique can be used to derive the S-parameters for the filter with little additional simulation time. These are the important features of the Modal analysis solver.

- Broadband calculation of S-parameters from the modal field distributions calculated using the eigenmode solver
- Re-normalization of S-parameters for specified port impedances
- Calculation of losses and Q-factors for each mode (perturbation method)
- Automatic parameter studies by using the built-in parameter sweep tool

- Automatic structure optimization for arbitrary goals by using the built-in optimizer

#### **4.3.4 Frequency Domain Solver**

The transient solver becomes less efficient for low frequency problems where the structure is much smaller than the shortest wavelength. In these cases it can be advantageous to solve the problem by using the frequency domain solver. This approach is most efficient when only a few frequency points are of interest. The important features of the Frequency domain solver are:

- Efficient calculation for loss-free and lossy structures including lossy wave guide ports
- Automatic fast broadband adaptive frequency sweep
- User defined frequency sweeps
- Direct and iterative matrix solvers with convergence acceleration techniques
- Port mode calculation by a 2D eigenmode solver in the frequency domain
- High performance radiating/absorbing boundary conditions
- Periodic boundary conditions including phase shift or scan angle
- Antenna farfield calculation (including gain, beam direction, side lobe suppression, etc.) with and without farfield approximation
- RCS calculation
- Calculation of SAR distributions
- Discrete elements (lumped resistors) as ports



Each of these solver's simulation results can then be visualized with a variety of different options. Again, a strongly interactive interface will help to quickly achieve the desired insight into a selected device. The last, but not the least, outstanding feature is the full parameterization of the structure modeler, which enables the use of variables in the definition of the selected device. In combination with the built-in optimizer and parameter sweep tools, CST Microwave Studio is capable of both the analysis and design of electromagnetic devices and hence can solve virtually any high frequency field problem.

## **CHAPTER 5**

### **RESEARCH APPROACH**

#### **5.1 Introduction**

The previous chapter introduced photodetectors, fundamentals of the EM waves, and previous work on MSM photodetectors. The basic simulation equation and the software used for analysis were also discussed. This chapter presents the methods and models used to simulate the MSM photodetector to study mechanisms for increased charge collection efficiency in sub-micron scale grated photodetectors. The charge collected is a function of the number of carriers produced in the active region of the detector, which in turn depends on the energy available to create electron-hole pairs in that region.

The semiconductor photodetector can be studied in terms of the energy deposited by an electromagnetic wave of an appropriate wavelength in the detector active region. Besides penetration of the electromagnetic wave, it is also important that the incident wave have energy equal to or greater than the material bandgap. This chapter deals with the electromagnetic field analysis to explain the collection efficiency of grated photodetectors. Increase in the collection efficiency for a given wavelength of the incoming electromagnetic signal is explained. A normal incident wave is considered for the analysis of the Si MSM detector by looking into the transmission of the electromagnetic wave field components as they travel through the grated walls into the device active region.

## 5.2 Analysis of Square and Wall like Grating Structures

For silicon detectors the wavelength of interest is 1100 nm, which corresponds to the bandgap energy. Thus, it is of interest to know why the grating structures aid in the deposition of more energy in the detector surface, thereby increasing carrier generation and collection. In the first simulation setup, a silicon substrate was placed in between two aluminum contacts as shown in the Fig 5.1. The dimension of the Si substrate was  $10 \times 10 \times 2 \mu\text{m}^3$ . The device was studied using a plane wave port (PWP) in the z direction with a continuous sinusoidal wave ( $\lambda$

$= 1100 \text{ nm}$ ) as an excitation signal as shown in Fig. 5.2. One can also use a double exponential pulse with an excitation equation given in (5.1) as the input signal, but a continuous sine

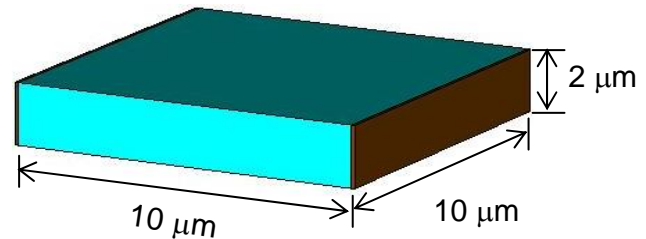


**Fig. 5.1 Simulated Structure without any gratings**

wave has been chosen in order to get a better view of the concept.

$$\text{Excitation Function} = -\exp(-E_1 \times \text{dtime}) + \exp(-E_2 \times \text{dtime}) \quad (5.1)$$

Where,  $E_1$  and  $E_2$  are constants.

$E$ -fields were calculated by placing the probe at the interface of the photodetector. Fig. 5.3 shows the  $E$ -field amplitude changes for a detector without any gratings as the EM wave reaches the surface of the detector.

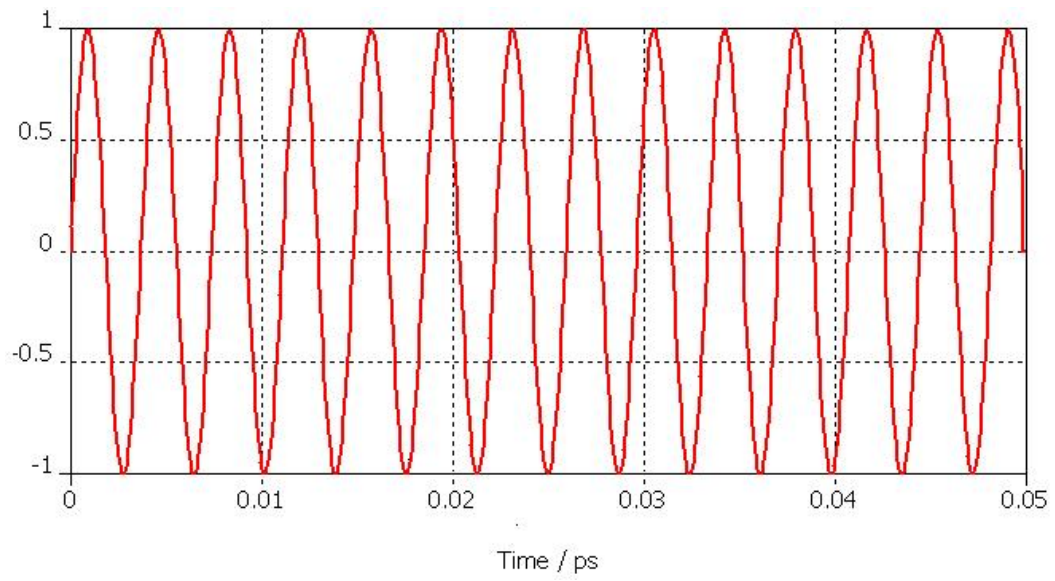


**Fig 5.2 Input Excitation Signal (Continuous Sine wave)**

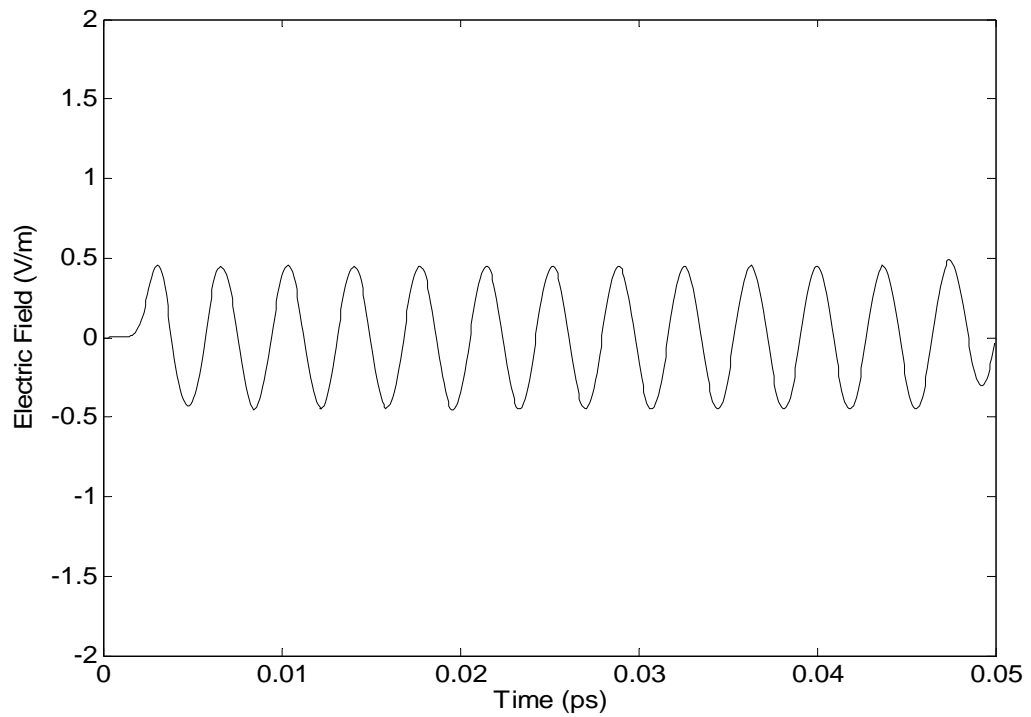


**Fig. 5.3 Incident wave amplitude changes as it travels through the surface of the detector without any gratings**

In the second simulation setup a silicon substrate was placed in between two aluminum contacts over which the Si sub-micron scale wall-like protrusions were placed, as shown in Fig. 5.4. The dimension of the Si substrate was  $10 \times 10 \times 2 \mu\text{m}^3$ . The dimension of the wall protrusion was  $1 \times 10 \times 1.2 \mu\text{m}^3$ . Another structure with square gratings was also created for comparison as shown in Fig. 5.4 (b).

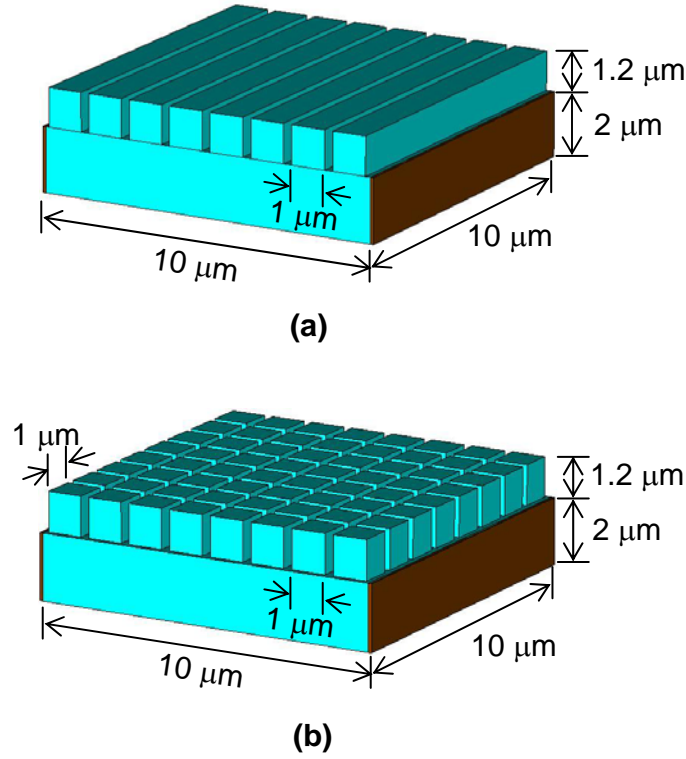


**Fig 5.4 Simulated Structure for (a) walls and, (b) square Gratings**

The square grating's dimension was  $1 \times 1 \times 1.2 \mu\text{m}^3$ . The device was studied using a plane wave port (PWP) in the z direction with a continuous sinusoidal wave ( $\lambda = 1.1 \mu\text{m}$ ) as an excitation signal. *E*-fields were calculated by placing the probes at the interface between the substrate and the Si protrusions (walls and squares).

Figure 5.5 shows the E-Field amplitude changes for a wall-like grating, and a detector without grating, as the incident electromagnetic wave travels from the restrictive grating region to the substrate region. The objective here was to compute the  $E$ -fields near the interface of the two regions as the electromagnetic pulse penetrates the protective layer towards the interior of the surface. Since there is a sudden change in the structure dimensions, a change in the impedances of the two areas would likely affect the

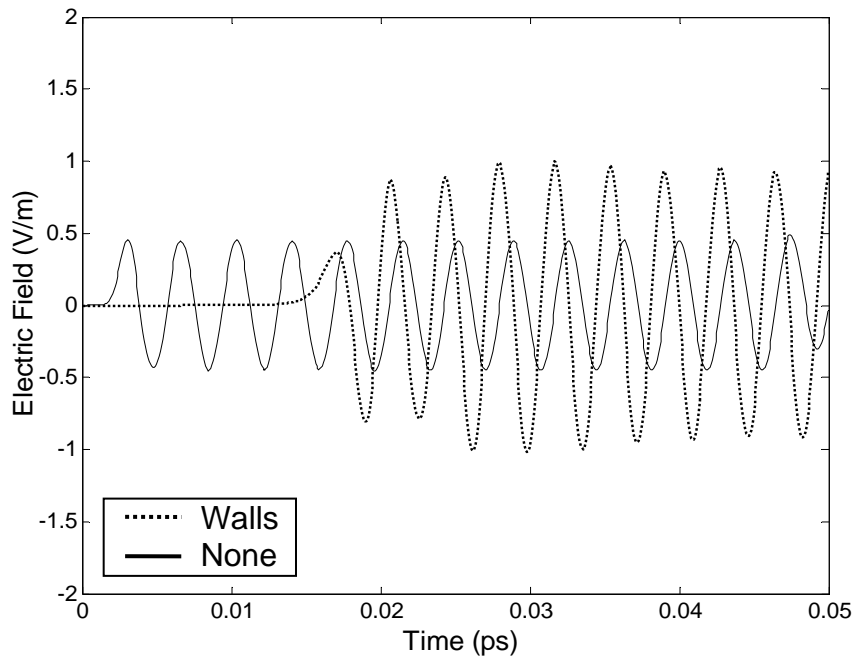


**Fig. 5.5 Incident wave amplitude changes as it travels from the wall-like grating to the substrate regions**

reflection and transmission data. The increase in amplitude is noticeable for the wall-like structure as shown in Fig. 5.4(a). Fig. 5.6 shows the transmitted wave amplitude using the square gratings as compared with the wall-like grating and a detector without any grating. It can be seen that there is higher amplitude for a square-shaped grating (Fig. 5.4 (b)) as compared to the wall-like structure.

A higher transmission coefficient value translates to more energy being transmitted to the substrate region from the grating region. Thus, there is higher energy transmission for the wall-like grating structure as compared to a detector without the gratings, as was reported in experiments [24].

Now,  $\tau = \frac{E_0^t}{E_0^i}$  increase in the transmission coefficient means an increase in the transmitted wave amplitude. This can be explained as follows: Consider two regions

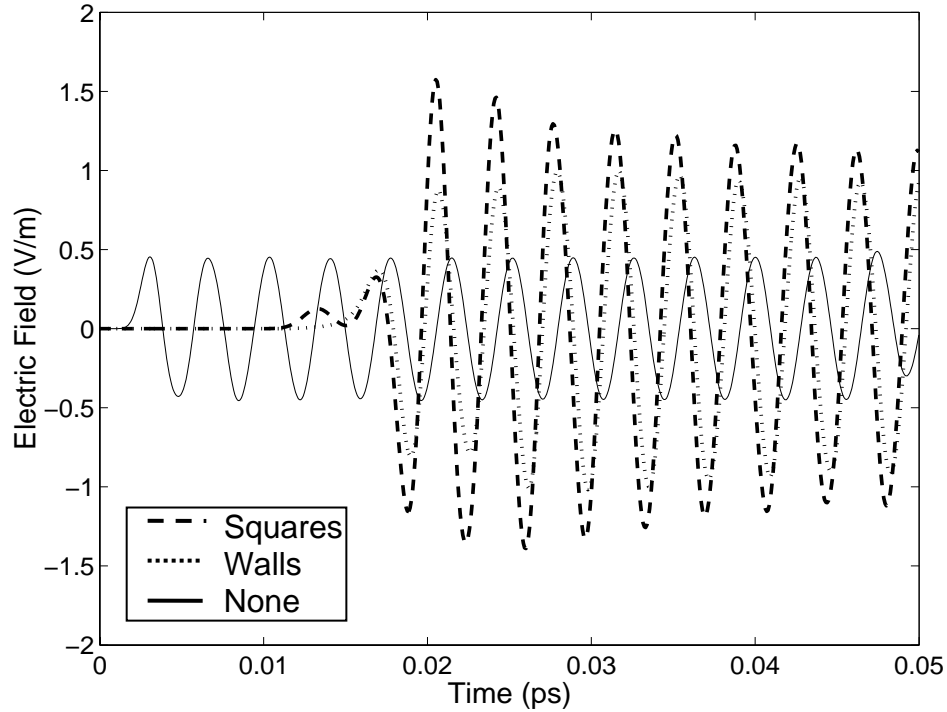


**Fig. 5.6 Incident wave amplitude changes as it travels from the square grating to the substrate regions**

(grating wall as region 1 and active area as region 2) of the detectors as shown in Fig 5.7. Assuming normal incidence from region 1 into region 2, the energy carried by the wave is distributed between the reflected and transmitted wave and can be characterized in

terms of the incident  $E$  field amplitude, reflection and transmission coefficients, and the impedances of the two media. The amplitude of the transmitted  $E$ -field can be explained in terms of conservation of the time averaged power (watts) due to  $\mathbf{E}$  and  $\mathbf{H}$  that are crossing a given surface  $A$  in the direction of the propagation.

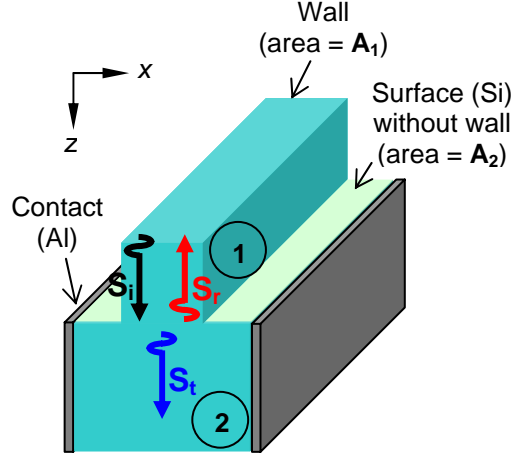


Fig 5.7 Single wall grating on the active region used for analysis

Starting from Eq. (2.54),

$$\langle P \rangle = \int_A \langle S \rangle \cdot dA = \langle S \rangle \cdot A \quad (5.2)$$

Where,  $\langle S \rangle$  is the average Poynting vector (watts/m<sup>2</sup>) derived from the instantaneous vector  $\vec{S}$  given by

$$\vec{S} = \vec{E} \times \vec{H} \quad (5.3)$$

When the wave is traveling from a region of cross sectional area  $A_1$  into a region of area  $A_2$  one can write relationships for incident, reflected and transmitted waves,



$$\langle P \rangle_1 = \langle S \rangle_i A_1 - \langle S \rangle_r A_1 \quad (5.4)$$

and

$$\langle P \rangle_2 = \langle S \rangle_t A_2 \quad (5.5)$$

Hence at the interface, one can write,

$$\begin{aligned} \langle S \rangle_i - \langle S \rangle_r &= \langle S \rangle_t \\ \frac{\langle P \rangle_i}{A_1} - |\Gamma|^2 \frac{\langle P \rangle_i}{A_1} &= \frac{\eta_1}{\eta_2} |\tau|^2 \frac{\langle P \rangle_i}{A_2} \\ \frac{\frac{\eta_1}{\eta_2} |\tau|^2}{1 - |\Gamma|^2} &= \frac{\frac{\eta_1}{\eta_2} |\tau|^2}{1 - |\tau - 1|^2} = \frac{A_2}{A_1} \end{aligned} \quad (5.6)$$

If the materials in region 1 are the same as in region 2 ( $\eta_1 = \eta_2$ ), and if we assume that  $A_2 > A_1$ , it follows from (5.6) that  $\tau > 1$ . Thus, the amplitude of the transmitted wave is greater than the amplitude of the incident wave, and an increase in  $\tau$  (where  $\tau = \frac{E'_0}{E_0^i}$ ) also translated to more energy deposition in the transmitted or the active region of the detector.

Thus, the wall-like structure produces a larger number of electron-hole pairs as compared to an MSM detector without the wall-like grating structure. It is expected that a square grating, which produces higher values for the transmission coefficient, will further improve the collection efficiency of the detectors. Therefore, the collection efficiency of the MSM detectors with square gratings should improve over the wall lattice gratings.

### 5.3 Analysis of Square Gratings with Change in Area

Until now, analysis shows improved efficiency for walls on the active area as compared to a bare active region. It is also shown that a square shaped grating has better efficiency than a wall lattice. The next step is to determine the number of square lattice that should occupy the active region for

higher efficiency. This is done by changing the area ( $A_1$ ), of the square Si extensions, while keeping the detector area ( $A_2$ ) constant. This means that the percentage of the area covered by

the Si extensions over the detector is changed. However, the number

of Si extensions over the detector was kept constant (64). Simulations were carried out using multitude number of areas ( $A_1$ ). The front view of the simulated structure is as shown in Figure 5.8.

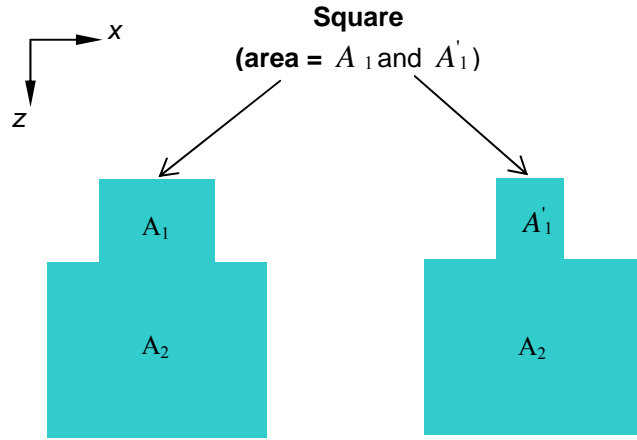


**Fig. 5.8 Front View of the Simulated Structure with different Si extension areas**

The dimension of the Si substrate was  $10 \times 10 \times 2 \mu\text{m}^3$ . The square grating dimensions were varied from  $1 \times 1 \times 1.2 \mu\text{m}^3$  ( $A_1$ ) to  $0.25 \times 0.25 \times 1.2 \mu\text{m}^3$  ( $A_1'$ ). As before, the device was studied using a plane wave port (PWP) in the z direction with a continuous sinusoidal wave ( $\lambda = 1.1 \mu\text{m}$ ) as an excitation signal. The comparison plot for the results is shown in Figure 5.9.

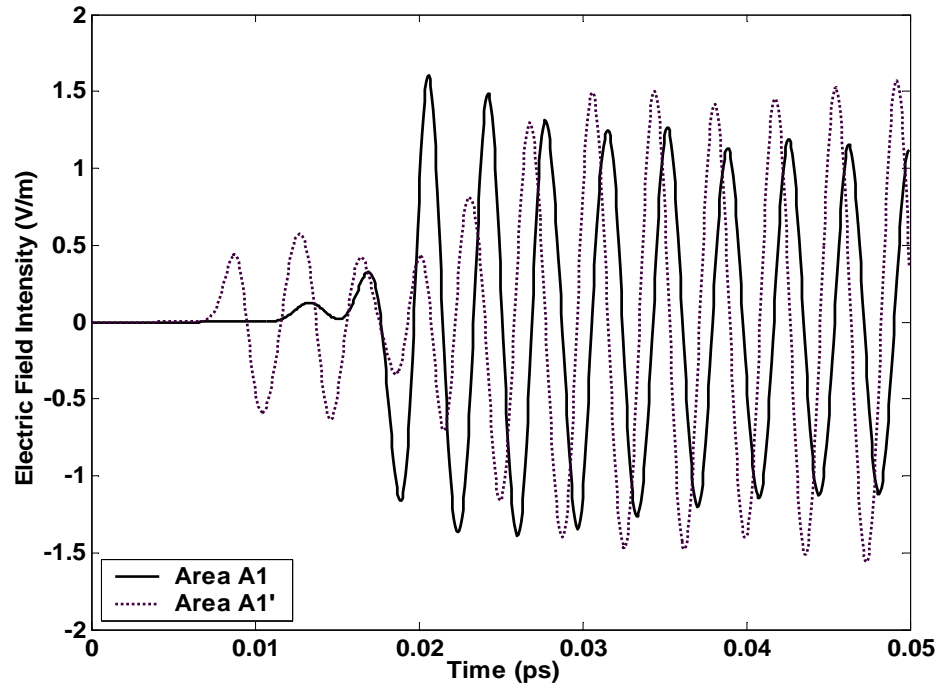


**Fig 5.9 Incident wave amplitude changes for a wave traveling through different Si extension areas**

From Fig. 5.9, it can be seen that as the area of the Si extension is decreased, the E-Field intensity is increased after it reaches the steady state. Here,

$$\frac{A_2}{A_1} < \frac{A_2}{A_1'} \quad (5.7)$$

Since  $A_2$  is constant and  $A_2 > A_1 > A_1'$ , it follows from Eq. (5.6),

$$\tau_{A_1'} > \tau_{A_1} \quad (5.8)$$

Where,  $\tau = \frac{E_0'}{E_0^i}$ ,

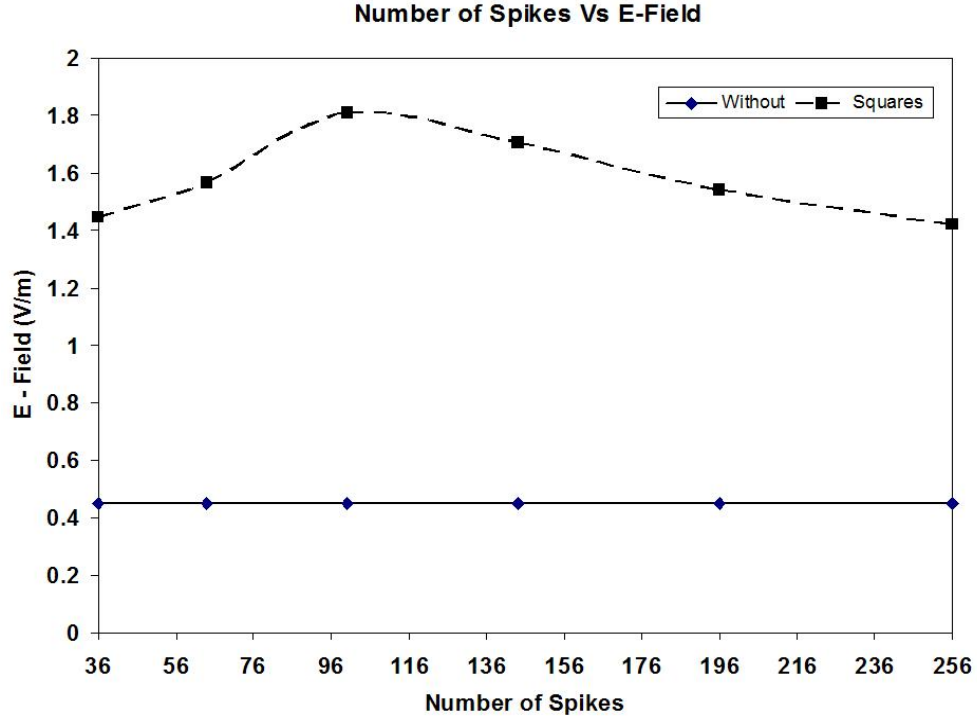


**Fig. 5.10 Plot of the E-Field Vs Number of Spikes**

It follows from Eq. 5.8 that a decrease in the area of the Si extension from  $A_1$  to  $A_1'$  increases the transmission coefficient,  $\tau$ . It means, in this case also, more energy is deposited in the transmitted or the active region of the detector. Hence, the electric field intensity is increased because there is a decrease in the area of each Si extension. Further simulations were done by changing the number of Si extensions on the detector. However, the area of the each Si extension is kept constant ( $0.25 \times 0.25 \times 1.2 \mu\text{m}^3$ ) because the highest E-Field has been obtained with this configuration. Simulations were carried out with 36, 64, 100, 144, 196 and 256 number of square Si extensions. It can be seen from Fig. 5.10 that as the number of Si extension increases, the Electric Field intensity increases. The solid line shows the E-Field without any Si extensions.

Hence, the maximum E-Field is obtained when the number of spikes is in between 90 and 110. With the increase in number of spikes, the percentage of area covered by the spikes on the detector increases. The ratio of the area covered by the Si spikes on the detector to the area uncovered starts to increase. Hence, the number of reflections due to the adjacent Si extensions increases, which account for the increase in the E-field. But after a certain critical percentage of the area covered by the Si extensions on the detector, the electric field starts to decrease as the number of reflections decrease. Hence, there exists a certain critical ratio of the area covered by the Si spikes on the detector to the area uncovered after which the E-field starts to decrease.

#### 5.4 Analysis of Cone like Grating Structures

The next step is to show an increase in the E-field intensity if the structure is changed to a cone lattice from a square lattice. Simulations were done with a fixed number of Si extensions (64), but this time, changing the square gratings to cones.

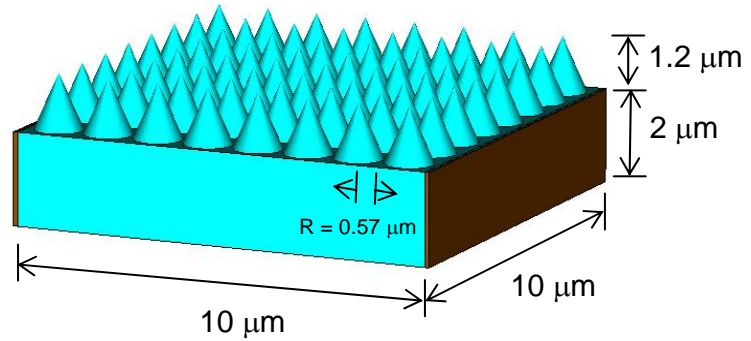


**Fig. 5.11 Simulated structure with cone gratings**

The structure simulated is shown in Fig. 5.11. The dimensions of the cone gratings were chosen such that the area covered by them on the detector is same as the area covered by the square gratings on the detector.

Figure 5.12 shows the variations in the amplitude of E-Fields for cone and square type gratings. It can be seen from the figure that the amplitude of the electric field intensity for cone grating is less than the electric field intensity for a square grating.

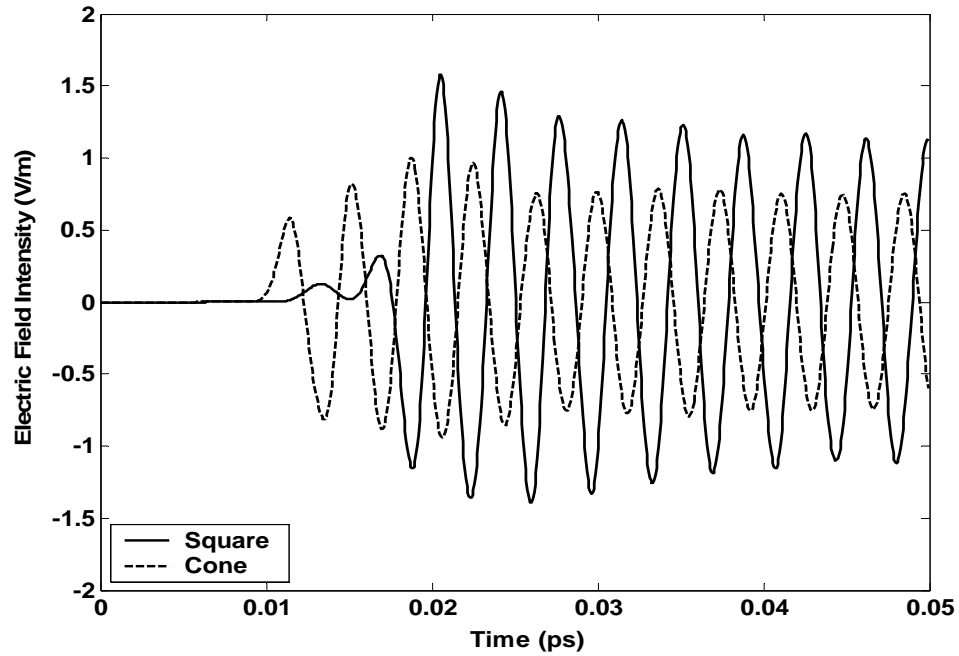


**Fig. 5.12 Incident wave amplitude changes as it travels through cone and square gratings**

To explain the difference between the cone and the square lattice, consider two cases for each structure. First consider the propagation of an EM wave at the surface of the grating and again consider the propagation of EM waves at the interface of the detector and the gratings.

In case of surface interactions, if a light ray is incident on a surface, part of the light is reflected and part may enter the second medium as the refracted ray, and may or may not undergo absorption there. Consider the case for the cone and square lattices shown in

Fig. 5.13. The amount of light reflected depends on the ratio of the refractive indices of the two media.

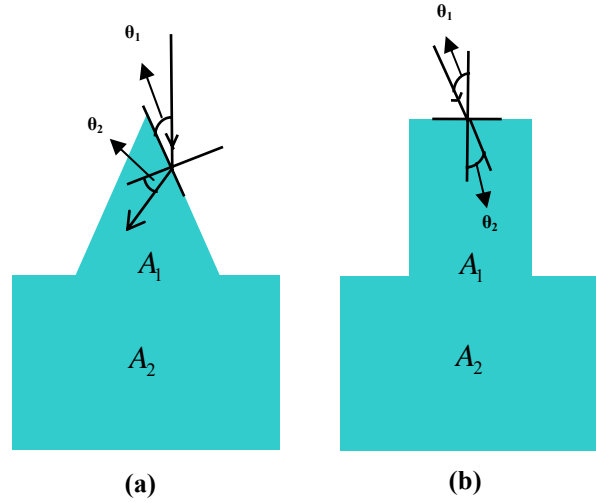


**Fig 5.13 Analysis of (a) Cone and, (b) Square grating structures**

Recall from Chapter 2, that if the wave travels from one medium to another (in this case from air to Si), we can apply an important law, called Snell's law, which states that the product of the refractive index and the sine of the angle of incidence of a ray in one medium is equal to the product of the refractive index and the sine of the angle of refraction in a successive medium. Algebraically, this can be written as

$$\eta_1 \sin \theta_1 = \eta_2 \sin \theta_2, \quad (5.9)$$

where,  $\eta_1$ ,  $\eta_2$  are the two values of refractive index and  $\theta_1$ ,  $\theta_2$  are the angles of incidence and refraction. The incident ray, the refracted ray, and the normal to the boundary at the point of incidence all lie in the same plane.

Generally, the refractive index of a denser transparent substance is higher than that of a less dense material; that is, the speed of light is lower in the denser substance. So, if a ray is incident on the surface, then a ray entering a medium with a higher refractive index, it will be bent towards the normal, and a ray entering a medium of lower refractive index will be bent away from the normal. Rays incident along the normal are reflected and refracted along the normal.

Fig 5.13 shows the front view of the propagation of the EM wave at the surface of the cone and square gratings. The area of the detector,  $A_2$  and the area covered by the grating on the detector,  $A_1$  are same for both the cone and the square. One can see from Fig. 5.13 (a) that as the electromagnetic wave is incident on the surface of the cone at an angle  $\theta_1$ , the refracted ray tends to move towards the normal. In our case  $\eta_1=1$ ,  $\eta_2=3.59$ . Hence, the ratio  $\eta_2/\eta_1 > 1$ . If it is assumed that the angle of incidence,  $\theta_1$  is constant, it follows from Eq. (5.9) that  $\theta_1 > \theta_2$ . Therefore, the angle of refraction  $\theta_2$  tends toward the normal and also away from the interface, after which, the wave may leak outside the cone grating. Hence, not all the energy of the EM wave crosses the interface. This accounts for the lesser efficiency of a cone shaped grating.

On the other hand, for the case of a square grating, it is a completely different situation. As the EM wave is incident on the surface of the square grating, the angle of refraction  $\theta_2$  bends toward the normal after which it travels toward the interface as shown in Fig. 5.13 (b). This accounts for the increase in the number of charge carriers at the interface. Hence, the overall charge collection efficiency of the detector with square gratings



increases. Thus, one can conclude that even though the interface area of the cone and the square lattice may be the same, but the amount of energy crossing the interface is much less for the cone.

## 5.5 Analysis of Square Gratings with Cladding

However, there is a possibility that the EM wave leaks away for the case of square gratings, but is less than that for a cone grating. Further simulations were done with doping around the gratings to prevent the leakage of the charges and for the higher power transmission into the active region thereby enhancing the collection efficiency due to the reflections from the surface.

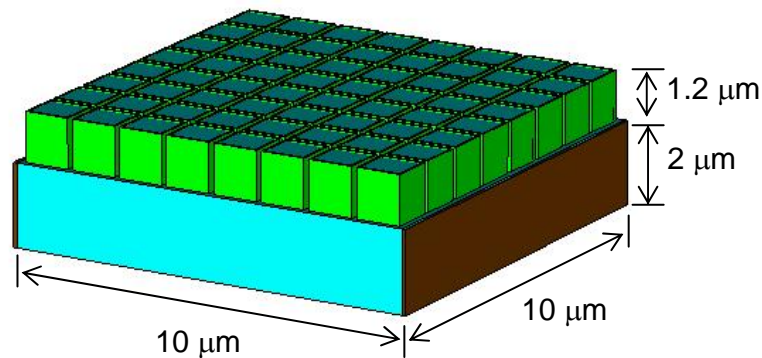


**Fig 5.14 Simulated Structure with doping around the square gratings**

Fig. 5.14 shows the structure simulated with all the dimensions of the detector surface and the gratings being the same as that of the earlier case, except that the square gratings are doped with a material of lower refractive index than Si. A thin layer of doping material is doped around the square gratings to increase the charge collection efficiency.

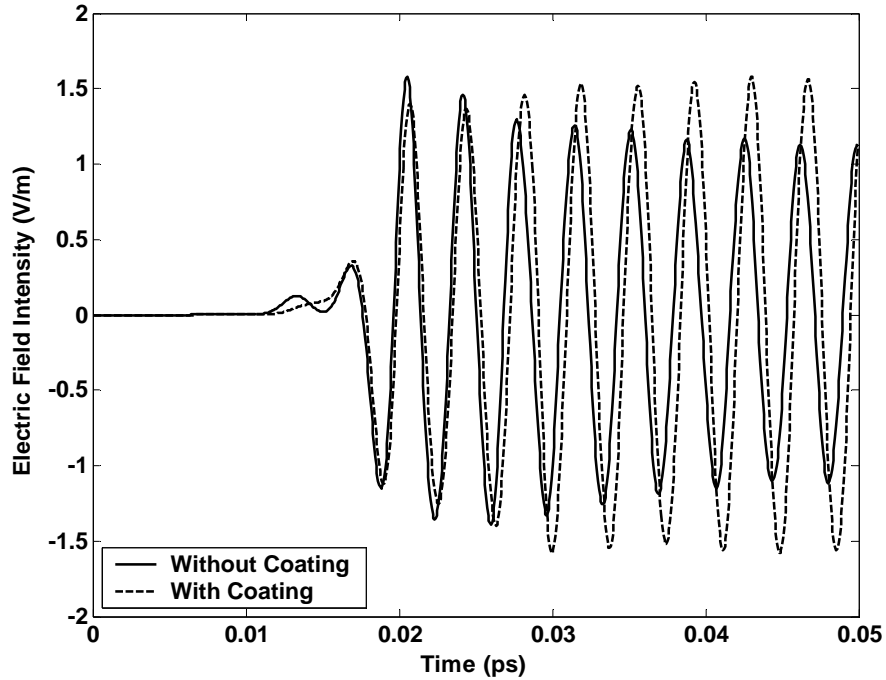


**Fig. 5.15 Incident wave amplitude changes as it travels through square gratings with and without doping (coating)**

Fig. 5.15 shows the simulated results for the case of square gratings with and without doping. It can be seen from the figure that there is an increase in the amplitude of the electric field intensity for the case of the square gratings with doping than the case without doping. Before going into the details, it is of importance to know the basics of fiber optics. First, a few equations related to optical fibers are derived and then applied to this study.

Fig 5.16 shows how the waves are guided along optical fibers. Light can be guided through thin dielectric rods made of glass or transparent plastic, known as optical fibers. Because the light is confined to traveling within the rod, the only loss in power is due to reflections at the sending and receiving ends of the fiber and absorption of the fiber

material (as it is not a perfect dielectric). The core here is Si with a refractive index  $\eta_{Si}$ . It is surrounded by a cladding with refractive index,  $\eta_c$ . where,  $\eta_c < \eta_{Si}$ . Also,  $\eta_0$  is the refractive index of the medium surrounding the fiber (in our case it is =1). When the wave is incident at an angle  $\theta_i$ , part of the wave is reflected and part of the wave is transmitted into the core with an angle,  $\theta_2$ . This wave is then incident to the cladding at an angle,  $\theta_3$  and again part of it is transmitted with an angle  $\theta_t$  into the cladding. The case of interest here is when  $\theta_t = \pi/2$ , where all the waves are reflected back into the core and no energy is transmitted into the cladding. To satisfy this condition of total internal reflection, the incident angle  $\theta_3$  in the core must be equal to or greater than the critical angle,  $\theta_c$  for the wave in the core medium incident upon the cladding medium.

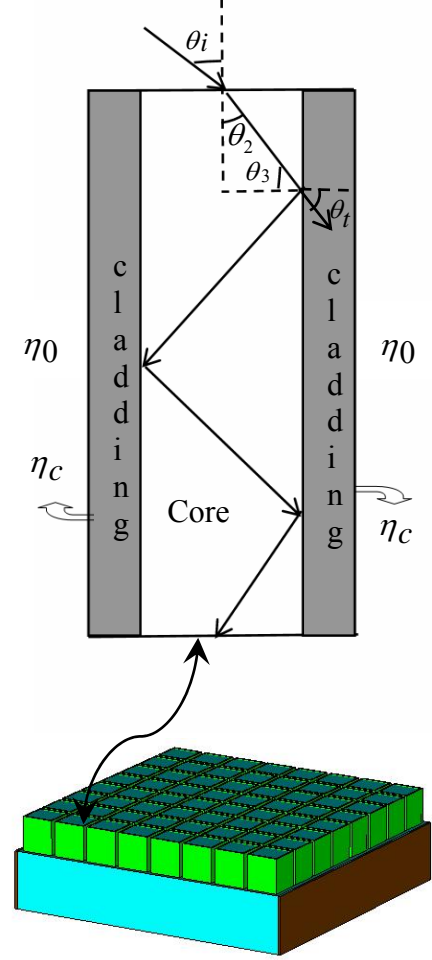


**Fig. 5.16 Guiding of waves in a square grating**

Recall Eq. (5.9) and substituting  $\theta_t = \pi/2$  we have,

$$\sin \theta_c = \frac{\eta_c}{\eta_{Si}} \quad (5.10)$$

To meet the total internal reflection requirement that  $\theta_3 \geq \theta_c$ , it is then necessary that

$\sin \theta_3 \geq \frac{\eta_c}{\eta_{Si}}$ . The angle  $\theta_2$  is the complement of angle  $\theta_3$ , and  $\cos \theta_2 = \sin \theta_3$ . Hence, the

necessary condition may be written as,

$$\cos \theta_2 \geq \frac{\eta_c}{\eta_{Si}}, \quad (5.11)$$

Moreover,  $\theta_2$  is related to the incidence angle on the face of the core,  $\theta_i$ , using Eq. (5.9),

$$\sin \theta_2 = \frac{\eta_0}{\eta_{Si}} \sin \theta_i, \quad (5.12)$$

where  $\eta_0$  is the refractive index of air, or

$$\cos \theta_2 = \left[ 1 - \left( \frac{\eta_0}{\eta_{Si}} \right)^2 \sin^2 \theta_i \right]^{\frac{1}{2}} \quad (5.13)$$

Using Eq. (5.13) on the left hand side of Eq. (5.11) and then solving for  $\sin \theta_i$  will give

$$\sin \theta_i \leq \frac{1}{\eta_0} (\eta_{Si}^2 - \eta_c^2)^{\frac{1}{2}} \quad (5.14)$$

The acceptance angle  $\theta_a$  is defined as the maximum value of  $\theta_i$  for which condition of total internal reflection remains satisfied.

$$\sin \theta_a = \frac{1}{\eta_0} (\eta_{Si}^2 - \eta_c^2)^{\frac{1}{2}} \quad (5.15)$$

Any ray of light incident upon the face of the core fiber at an incidence angle within the acceptance cone can propagate down the core. This means that there can be a large number of ray paths, called modes, by which light energy can travel in the core. In this case, assume the optimum acceptance angle,  $\theta_a = 35^\circ$ . The refractive indices for silicon and air are  $\eta_{si} = 3.59$  and  $\eta_0 = 1$  respectively. After, substituting these values into Eq. (5.15), the required refractive index of the cladding,  $\eta_c$  turns out to be 3.54.

This refractive index for the cladding was used in the simulations so that all of the light that is incident on the square gratings gets reflected back into the detector without any leakage. Hence, large amounts of energy get deposited at the detector's active region leading to an increase in the concentration efficiency of the photodetector.

## **CHAPTER 6**

### **CONCLUSIONS**

The main objective of this research was to study the enhanced charge collection mechanisms of a metal-semiconductor-metal (MSM) photodetector with gratings. The increase in the collection efficiency due to sub-micron scale wall-like silicon gratings on the active surface of the detector was studied. The transmission of electromagnetic energy due to structural changes at the interface accounts for higher transmitted energy and the subsequent generation and collection of carriers at the interface, thus contributing to enhanced collection efficiency. Simulations were done using a sinusoidal wave as the excitation signal on the MSM photodetector with walls as grating and without any gratings. It is shown that there is an increase in the amplitude of the electric field intensity for the case of wall-like Si gratings when compared to the detector without any gratings.

It was also demonstrated that rearranging the wall structures to a square lattice could improve the collection efficiency further. Variations in the amplitude of the electric field intensity for the case of a photodetector with square gratings were determined. It was shown that there is an increase in the collection efficiency of the photodetector with square gratings as compared to the efficiency of the detector without any gratings or with wall-like gratings.

Results were obtained by changing the percentage of the area covered by the square Si gratings on the detector. It was shown that there is an increase in the amplitude of the electric field intensity as the percentage of the area covered by the Si gratings on the detector decreases. Simulations were done by varying the number of Si spikes covered on the detector. It is shown that as the number of spikes increases, the amplitude of the electric field intensity increases to a maximum then starts to decrease. Hence, it can be concluded that there exists a certain critical ratio of the percentage of the area covered by the gratings to the area uncovered over the detector after which the amplitude of the electric field intensity starts to decrease.

Simulations were done on the photodetector with cone shaped Si gratings. It was shown how the incident wave leaks away from the surface of the grating. Hence, a very little amount of energy is accumulated at the interface which accounts for a lesser efficiency. However, for the case of square Si gratings, there is a less possibility that the wave leaks away from the grating. For higher power transmission into the active region, the square Si gratings were doped with a material of refractive index lesser than that of the Si, so that almost the entire incident wave is reflected towards the interface.

The scope of further studies is to determine the grating structure that will yield a collection efficiency greater than that of the square gratings. Also, it is of interest to find the evanescent field modes as the structure dimension changes and their contribution to the total collection efficiency.

## REFERENCES

- [1] Fawwaz T. Ulaby, "Fundamentals of Applied Electromagnetics," Prentice Hall, NJ, USA, 2004.
- [2] K. Kato, "Ultrawide-band/high-frequency photodetectors," *IEEE Trans. Microwave Theory Tech.*, vol. 47, pp. 1265–1281, July 1999.
- [3] J. B. D. Soole and H. Schumacher, "Transit-time limited frequency response of InGaAs MSM photodetectors", *IEEE Trans. Electron Devices*, vol. 37 (11), pp. 2285–2291, Nov. 1990.
- [4] R. G. DeCorby, A. J.P. Hnatiw, J. N. McMullin, "Techniques to Improve Speed and Efficiency of Photodetectors," *Proc. of the IEEE Canadian Conference on Electrical and Computer Engineering*, Shaw Conference Center, Edmonton, Alberta, Canada, May 9-12, 1999.
- [5] T. Sugeta, T. Urisu, S. Sakata and Y. Mizushima, "Metal-semiconductor-metal photodetector for high-speed optoelectronic circuits," *Proc. 11<sup>th</sup> Conf. (1979 Int.), Solid State Devices, Tokyo*, 1979, Japanese J. Appl. Phys., Supp. 19-1, 459 (1980).
- [6] J. F. Holzman, F. E. Vermeulen, and A. Y. Elezzabi, "Ultrafast photoconductive self-switching of subpicosecond electrical pulses," *IEEE J. Quan. Electron.*, vol. 36, pp. 130–136, Feb. 2000.
- [7] E. Sano, "A device model for metal-semiconductor-metal photodetectors and its application to optoelectronic integrated circuit simulation," *IEEE. Trans. Electron Devices*, 37 (9), pp. 1964–1968, Sep. 1990.
- [8] M. Ghioni, F. Zappa, V. P. Kesan, and J. Warnock, "A VLSI-compatible high-speed silicon photodetector for optical data link applications," *IEEE Trans. Electron Devices*, vol. 43 (7), pp. 1054-1060, July 1996.
- [9] J. S. Wang, C. G. Shih, W. H. Chang, J. R. Middleton, P. A. Apostolakis, and M. Feng, "11-GHz bandwidth optical integrated receivers using GaAs MESFET and MSM technology," *IEEE Phot. Tech. Lett.*, vol. 5, pp. 316–318, 1993.
- [10] A. Sayles and J. Uyemura, "An optoelectronic CMOS memory circuit for parallel detection and storage of optical data," *IEEE J. Solid-State Circuits*, vol. 23, pp. 1110–1115, 1991.



- [11] M. Caria, L. Barberini, S. Cadeddu, A. Giannattasio, A. Lai, A. Rusani, A. Sesselego, "Far UV responsivity of commercial silicon photodetectors," *Nuclear Instruments and Methods in Physics Research A*, 466 (2001) 115–118.
- [12] M. Y. Liu, E. Chen, and S. Y. Chou, "140 GHz metal-semiconductor-metal photodetectors on silicon-on-insulator substrate with a scaled layer," *Appl. Phys. Lett.*, Vol. 65, pp. 887-888, 1994.
- [13] H. C. Lee and B. V. Zeghbroeck, "A novel high-speed silicon MSM photodetector operating at 830 nm wavelength," *IEEE Trans. Electron. Devices*, vol. 16, pp. 175-177, 1995.
- [14] N. F. Mott and E. A. Davis, "Electronic Processes in Noncrystalline Materials," 2<sup>nd</sup> ed., Oxford Univ. Press, Oxford, U.K., 1979.
- [15] Qing Z. Liu, R. Ian MacDonald, "Controlled Nonlinearity Monolithic Integrated Optoelectronic Mixing Receiver," *IEEE Phot. Tech. Lett.*, vol. 5 (12), pp. 1403-1406, Dec.1993.
- [16] P. H. Shen *et al.*, "Interdigitated finger semiconductor photodetector for optoelectronic mixing," *Proc. SPIE*, vol. 4028, pp. 426–435, July 2000.
- [17] Y. Liu, W. Khalil, P. B. Fischer, S. Y. Chou, T. Y. Hsiang, S. Alexandrou, R. Sobolewski, "Nanoscale Ultrafast Metal-Semiconductor-Metal Photodetectors," *50th Annual Device Research Conference*, pp. 162-163, June 22-24, 1992.
- [18] J. J. Kuta *et al.*, "Polarization and wavelength dependence of metal-semiconductor-metal Photodetector response," *Appl. Phys. Lett.*, vol. 64 (2), Jan 1994.
- [19] Jinwook Burm *et al.*, "High-Frequency, High-Efficiency MSM Photodetectors," *IEEE J. Quan. Electronics*, vol. 31(8), Aug 1995.
- [20] K. Kishino, M. S. Ünlü, J. I. Chyi, J. Reed, L. Arsenault, and H. Morkoc, "Resonant cavity-enhanced (RCE) photodetectors," *IEEE J. Quan. Electronics*, vol. 27 (8), pp. 2025-2034, Aug. 1991.
- [21] Y. L. Ho and K. S. Wong, "Bandwidth enhancement in Si metal-semiconductor-metal photodetectors by trench formation," *IEEE Phot. Tech. Lett.*, vol. 8, No. 8, pp. 1064-1066, 1996.
- [22] L. H. Lai, T. C. Chang, Y. A. Chen, W. C. Tsay, and J. W. Hong, "Characteristics of MSM photodiodes with trench electrodes on p-type Si wafer," *IEEE Trans. on Electron. Devices*, vol. 45, pp. 2018-2023, 1998.

- [23] A. K. Sharma, K. A. M. Scott, S. R. J. Brueck, J. C. Zolper, D. R. Myers, "Ion Implantation Enhanced Metal-Si-Metal Photodetectors," *IEEE Phot. Tech. Lett.*, vol. 6 (5), May 1994.
- [24] A. K. Sharma, S. H. Zaidi, P. C. Logoftu, and S. R. J. Brueck, "Optical and Electrical Properties of Nanostructured Metal-Silicon-Metal Photodetectors," *IEEE J. Quant. Electronics*, vol. 38, no. 12, pp. 1651-1660, 2002.
- [25] Stéphane Collin, Fabrice Pardo, Roland Teissier, and Jean-Luc Pelouard, "Efficient light absorption in metal–semiconductor–metal nanostructures", *Appl. Phys. Lett.*, vol. 85(2), July 2004.
- [26] Sang-Woo Seo et al., "High-Speed Large-Area Inverted InGaAs Thin-Film Metal–Semiconductor–Metal Photodetectors," *IEEE J. of Selected Topics in Quant. Electronics*, vol. 10, no. 4, July/August 2004.
- [27] K. S. Yee, "Numerical Solution of Initial Boundary Value Problems Involving Maxwell's Equations in Isotropic Media," *IEEE Trans. on Antennas and Propagation*, vol. 14, no. 3, pp. 302-307, Mar 1966.
- [28] T. Weiland, "A discretization method for the solution of Maxwell's equations for Six-component fields," *Electronics and Communication, AEU*, vol. 31, no. 3, pp.116-120, 1977.
- [29] Manual, CST Microwave Studio 5.0, 2004.
- [30] T. Weiland, "Time Domain Electromagnetic Field Computation with Finite Difference Methods," *International J. of Numerical Modeling*, vol. 9, pp. 295-319, 1996.